Journal of Computational Physics 230 (2011) 4696–4722

Contents lists available at ScienceDirect

Journal of Computational Physics

journal homepage: www.elsevier.com/locate/jcp

A stochastic mixed finite element heterogeneous multiscale method for flow in porous media

Xiang Ma, Nicholas Zabaras *

Materials Process Design and Control Laboratory, Sibley School of Mechanical and Aerospace Engineering, 101 Frank H.T. Rhodes Hall, Cornell University, Ithaca, NY 14853-3801, USA

ARTICLE INFO

Article history:
Received 1 August 2010
Received in revised form 28 February 2011
Accepted 1 March 2011
Available online 4 March 2011

Keywords:
Stochastic partial differential equations
Flow in porous media
Stochastic multiscale method
Mixed finite element method
High dimensional model representation
Stochastic collocation method
Sparse grids
Adaptivity

ABSTRACT

A computational methodology is developed to efficiently perform uncertainty quantification for fluid transport in porous media in the presence of both stochastic permeability and multiple scales. In order to capture the small scale heterogeneity, a new mixed multiscale finite element method is developed within the framework of the heterogeneous multiscale method (HMM) in the spatial domain. This new method ensures both local and global mass conservation. Starting from a specified covariance function, the stochastic log-permeability is discretized in the stochastic space using a truncated Karhunen–Loève expansion with several random variables. Due to the small correlation length of the covariance function, this often results in a high stochastic dimensionality. Therefore, a newly developed adaptive high dimensional stochastic model representation technique (HDMR) is used in the stochastic space. This results in a set of low stochastic dimensional subproblems which are efficiently solved using the adaptive sparse grid collocation method (ASGC). Numerical examples are presented for both deterministic and stochastic permeability to show the accuracy and efficiency of the developed stochastic multiscale method.

1. Introduction

Flow through porous media is ubiquitous, occurring from large geological scales down to microscopic scales. Several critical engineering phenomena like contaminant spread, nuclear waste disposal and oil recovery rely on accurate analysis and prediction of these multiscale phenomena. Such analysis is complicated by heterogeneities at various length scales as well as inherent uncertainties. For these reasons in order to predict the flow and transport in stochastic porous media, some type of stochastic upscaling or coarsening is needed for computational efficiency by solving these problems on a coarse grid. However, most of the existing multiscale methods are realization based, i.e. they can only solve a deterministic problem for a single realization of the stochastic permeability field. This is not sufficient for uncertainty quantification since we are mostly interested in the statistics of the flow behavior, such as mean and standard deviation. In this paper, we propose a stochastic multiscale approach which resolves both uncertainties and subgrid scales by developing a new multiscale method and adopting a newly developed adaptive high dimensional stochastic model representation technique (HDMR). The goal of the multiscale method is to coarsen the flow equations spatially whereas HDMR is used to address the curse of dimensionality in high dimensional stochastic spaces.

One of the challenging mathematical issues in the analysis of transport through heterogeneous random media is the multiscale nature of the property variations. Complete response evaluation involving full-scale spatial and temporal resolution

* Corresponding author. Fax: +1 607 255 1222.
E-mail address: zabaras@cornell.edu (N. Zabaras).
URL: http://mpdc.mae.cornell.edu/ (N. Zabaras).

0021-9991/$ - see front matter © 2011 Elsevier Inc. All rights reserved.
doi:10.1016/j.jcp.2011.03.001

simulations of multiscale systems is extremely expensive. Computational techniques have been developed that solve for an appropriate coarse-scale problem that captures the effect of the subgrid-scales. The most popular techniques developed for such upscaling fall under the category of multiscale methods viz. the multiscale finite element (MsFEM) method [1–3], the variational multiscale (VMS) method [4,5] and the heterogeneous multiscale (HMM) method [6,7]. The MsFEM was originally developed in [1,2] for the solution of elliptic equation based problems with multiscale coefficients using conforming linear finite elements. The primal unknown is the nodal value, e.g. the pressure, and one can obtain the velocity by calculating the gradient of the pressure field given the finite element solution. The result is generally not accurate and conservation of the flux in each element may be violated, which is an important property for the numerical solution of transport equations in porous media. Therefore, a mixed multiscale finite element method (MMsFEM) that guarantees the local mass conservation at the element level was proposed in [8] using the lowest-order Raviart–Thomas mixed finite element [9]. The basic idea of the method is to construct the multiscale finite element basis functions that incorporate the small scale information through the solution of a local problem in each element and couple them through a global formulation of the problem. However, this work only produces a globally mass conserving velocity field. This work was extended in a number of important ways to guarantee mass conservation on both fine- and coarse-scales [10,11]. A similar framework utilizing the finite volume method as the global solver was also proposed in [12–14], which also preserves mass conservation at both scales. The basic idea of the VMS method is to invoke a multiscale split of the solution into a coarse-scale part and a subgrid component. The variational coarse-scale problem is performed and solved using the solution of the localized subgrid problem. Parallel to MMsFEM, a mixed finite element version of VMS was also proposed in [15–17], which is often called "Numerical subgrid upscaling". A thorough comparison of the above three methods for elliptic problems in porous media flows can be found in [18].

HMM is a more general methodology for multiscale PDEs (see [7] for a review). The basic idea of HMM consists of two components: selection of a macroscopic solver and estimating the needed macroscale data by solving locally the fine-scale problem. It allows two different sets of governing equations on macro- and micro-scales, e.g. atomistic simulation on micro-scale and continuum simulation on macro-scale [19,20]. This framework was utilized to solve multiscale elliptic problems with the conforming linear FEM (FeHMM) [21–23]. The method was analyzed in a series of papers [24–26]. However, unlike the MMsFEM, there is no discussion of the mixed version of FeHMM except the work in [27], where the author first developed the theory of the mixed finite element version of HMM for the elliptic problem and proved the stability and convergence of this new method in the case of periodic coefficients. However, the theory in [27] is not suitable for realistic problems such as flow through porous media since the permeability field is usually not periodic. In addition, no numerical implementation was given in [27]. Motivated by the work in [27], in this paper, we first develop and implement the mixed finite element version of HMM with application to flow transport in heterogeneous porous media, which we will call it mixed heterogeneous multiscale method (MxHMM).

All of the above mentioned multiscale analyses of such systems inherently assume that the complete multiscale variation of the permeability is known. This assumption limits the applicability of these frameworks since it is usually not possible to experimentally determine the complete structure of the media at small scales. One way to cope with this difficulty is to view the permeability variation as a random field that satisfies certain statistical correlations. This naturally results in describing the physical phenomena using stochastic partial differential equations (SPDEs). The development of efficient stochastic methods that are applicable for flow in porous media has drawn significant interest in the last few years. Several techniques like generalized polynomial chaos expansions (gPC) [28–30], perturbation/moment equation methods [31–34] and stochastic collocation method [32,35–38] have been considered. Among these methods, the collocation methods share the fast convergence of the gPC method while having the decoupled nature of Monte Carlo (MC) sampling. This framework represents the stochastic solution as a polynomial approximation. This interpolant is constructed via independent function calls to the deterministic problem solver at different interpolation points which are selected based on special rules. Choice of collocation points include tensor product of zeros of orthogonal polynomials [35,39] or sparse grid approximations [40–42]. It is well known that the global polynomial interpolation cannot resolve local discontinuity in the stochastic space. Its convergence rate still exhibits a logarithmic dependence on the dimension. For high-dimensional problems, a higher-interpolation level is required to achieve a satisfactory accuracy. However, at the same time, the number of collocation points required increases exponentially for high-dimensional problems (>10). Therefore, its computational cost becomes quickly intractable. This method is still limited to a moderate number of random variables (5–10). To this end, Ma and Zabaras [43] extended this methodology to adaptive sparse grid collocation (ASGC). This method utilizes local linear interpolation and uses the magnitude of the hierarchical surplus as an error indicator to detect the non-smooth region in the stochastic space and thus place automatically more points around this region. This approach results in further computational gains and guarantees that a user-defined error threshold is met. However, this method is still not suitable for heterogeneous porous media with small correlation length leading to high stochastic dimensionality. In recent work, Ma and Zabaras [44] combined the ASGC with the adaptive stochastic high dimensional model representation (HDMR) technique [45]. HDMR represents the model outputs as a finite hierarchical correlated function expansion in terms of the stochastic inputs starting from lower-order to higher-order component functions. HDMR is efficient at capturing the high-dimensional input–output relationship such that the behavior for many physical systems can be modeled to a good accuracy only by the first few lower-order terms. An adaptive version of HDMR is also developed to automatically detect the important dimensions and construct higher-order terms using only the important dimensions. The heterogeneity of the porous media is often due to the small correlation length of the covariance structure. All the above mentioned works did not take into account the multiscale nature of the permeability.

Therefore, in this work, we will use both of these developments in the stochastic space together with the newly developed MxHMM for the spatial discretization.

There exist several new stochastic multiscale methods for elliptic problems. In [46] and [47], the variational multiscale method was extended to a stochastic version using gPC and stochastic collocation method respectively to solve a simple diffusion problem. The stochastic multiscale finite element was also developed in [48] however only an elliptic problem was solved to find the hydraulic head. More related work can be found in [49–51]. In [49], the stochastic numerical subgrid upscaling method was also developed for the solution of the mixed form of the Darcy's equation using the stochastic collocation method. However, in that work, only the statistics of the coarse-scale velocity and pressure were solved and no flow transport problem was investigated. In [50], a projection method for the solution of the stochastic mixed multiscale finite element method was introduced where the velocity solution was projected onto multiscale velocity basis functions which are precomputed using a set of realizations of the stochastic permeability field. It generally involves the solution of a large linear system of equations to find the projection coefficients if the number of realizations is large. For each new permeability sample, this method needs to solve one coarse-scale problem again and is generally computationally expensive. In addition, the MC method is used to compute the statistics of the solution. In [51], this framework was used to sample the permeability given measurements within the Markov chain Monte Carlo method (MCMC) framework and again no statistics of the saturation were reported. However, in our application, we are primarily interested in mean behavior and a measure of uncertainty, e.g. standard deviation, in the saturation of each phase. By using the adaptive HDMR and ASGC developed in [44], we can obtain not only a surrogate model for the saturation profile but also can easily extract the statistics of the saturation. Therefore, the novel contributions of this paper are as follows: (1) we develop a new mixed finite element version of the heterogeneous multiscale method for the simulation of flow through porous media in the spatial domain; (2) we utilize the newly developed HDMR technique to address the *curse of dimensionality* that occurs naturally in this problem due to the heterogeneity of the permeability; (3) finally, we investigate the effect of the stochastic permeability on various statistics of the saturation using the recently developed adaptive HDMR method.

This paper is organized as follows: In the next section, the mathematical framework of stochastic porous media flow problem in the mixed form is considered. In Section 3.1, the ASGC and HDMR methods for solving SPDEs are briefly reviewed. In Section 4, the theory of MxHMM is developed. Various examples with deterministic and stochastic permeability are given in Section 5. Finally, concluding remarks are provided in Section 6.

2. Problem definition

In this section, we follow the notation in [43]. Let us define a complete probability space $(\Omega, \mathcal{F}, \mathcal{P})$ with sample space Ω which corresponds to the outcomes of some experiments, $\mathcal{F} \subset 2^{\Omega}$ is the σ-algebra of subsets in Ω and $\mathcal{P} : \mathcal{F} \to [0,1]$ is the probability measure. Also, let us define D as a d-dimensional bounded domain $D \subset \mathbb{R}^d$ $(d = 2, 3)$ with boundary ∂D. The governing equations for immiscible and incompressible two-phase flow in porous media consists of an elliptic equation for fluid pressure and a transport equation for the movement of fluid phases. For simplicity, we will neglect the effects from gravity, capillary forces and assume that the porosity is a constant. The two phases will be referred to as water and oil, denoted as w and o, respectively. The total Darcy velocity $\boldsymbol{u}$ and the pressure p satisfy for $\mathcal{P}$-almost everywhere (a.e.) in Ω the following SPDEs [18]

$$\nabla \cdot \boldsymbol{u} = \bar{q}, \quad \boldsymbol{u} = -K(\boldsymbol{x}, \omega)\lambda_t \nabla p, \quad \forall \boldsymbol{x} \in D, \tag{1}$$

with the following boundary conditions

$$p = \bar{p} \text{ on } \partial D_p, \quad \boldsymbol{u} \cdot \boldsymbol{n} = \bar{\boldsymbol{u}} \text{ on } \partial D_u. \tag{2}$$

The total velocity $\boldsymbol{u} = \boldsymbol{u}_o + \boldsymbol{u}_w$ is a sum of the velocities of oil $\boldsymbol{u}_o$ and water $\boldsymbol{u}_w$. $\bar{q}$ is a volumetric source term which is assumed 0 throughout the paper. The random permeability tensor K is assumed to be diagonal and uniformly positive definite. In addition, we will assume K is a stochastic scalar function. The total mobility is given by $\lambda_t = \lambda_w + \lambda_o$, where λ_i models the reduced mobility of phase i due to the presence of the other phase. Without loss of generality, we assume that the boundary conditions are deterministic and that the Neumman condition is homogeneous, $\bar{\boldsymbol{u}} = 0$ on ∂D_u.

Furthermore, to assess the quality of the multiscale model, the unit mobility ratio displacement model is used, i.e. $\lambda_w = S$, $\lambda_o = 1 - S$ and hence $\lambda_t = 1$, where S is the water saturation. Under these assumptions, the water saturation equation is given by

$$\frac{\partial S(\boldsymbol{x}, t, \omega)}{\partial t} + \boldsymbol{u} \cdot \nabla S(\boldsymbol{x}, t, \omega) = 0, \quad \forall \boldsymbol{x} \in D, \ t \in [0, T]. \tag{3}$$

Since the permeability K is a stochastic function, all the unknowns p, $\boldsymbol{u}$ and S are also stochastic. Therefore, our complete stochastic model is: find stochastic functions $\boldsymbol{u} : \Omega \times D \to \mathbb{R}$, $p : \Omega \times D \to \mathbb{R}$ and $S : \Omega \times [0, T] \times D \to \mathbb{R}$ for $\mathcal{P}$-almost everywhere (a.e.) $\omega \in \Omega$ such that the following equations hold:

$$\nabla \cdot \boldsymbol{u}(\boldsymbol{x}, \omega) = 0, \quad \boldsymbol{u}(\boldsymbol{x}, \omega) = -K(\boldsymbol{x}, \omega)\nabla p(\boldsymbol{x}, \omega) \quad \forall \boldsymbol{x} \in D, \tag{4}$$

$$\frac{\partial S(\boldsymbol{x}, t, \omega)}{\partial t} + \boldsymbol{u}(\boldsymbol{x}, t, \omega) \cdot \nabla S(\boldsymbol{x}, t, \omega) = 0, \quad \forall \boldsymbol{x} \in D, \ t \in [0, T], \tag{5}$$

with the boundary conditions

$$p = \bar{p} \text{ on } \partial D_p, \quad \boldsymbol{u}\cdot\boldsymbol{n} = 0 \text{ on } \partial D_u, \tag{6}$$

together with appropriate initial and boundary conditions for S. Computation with this model is much more efficient than using the actual two-phase flow model because the pressure and saturation equations are effectively decoupled. Throughout this paper, the Darcy velocity $\boldsymbol{u}$ is first computed using the mixed finite element heterogeneous multiscale method developed in Section 4.1 and then the saturation equation is solved using a upwinding finite element scheme [52] in Section 4.2. Although these equations differ from the actual flow equations, they do capture many important aspects of two-phase flow problems. Specifically, the effects of the heterogeneity are often similar in the unit mobility and two-phase flow problems [53].

Geostatistical models often suggest that the permeability field is a weakly stationary second-order random field such that the mean log-permeability is constant and its covariance function only depends on the relative distance of two points rather than their actual location [8]. Denote $G(\boldsymbol{x},\omega) = \log(K)$. We employ the 'finite-dimensional noise assumption' [40] and using the Karhunen–Loève (K–L) expansion [54] we approximate $G(\boldsymbol{x},\omega)$ with a finite-dimensional representation:

$$G(\boldsymbol{x},\omega) = \mathbb{E}[G(\boldsymbol{x})] + \sum_{i=1}^{N} \sqrt{\lambda_i}\phi_i(\boldsymbol{x})Y_i(\omega), \tag{7}$$

where $\{Y_i(\omega)\}_{i=1}^N$ are uncorrelated random variables. Also, $\phi_i(\boldsymbol{x})$ and λ_i are the eigenfunctions and eigenvalues of the covariance function, respectively.

When using the K–L expansion, we here assume that we obtain a set of mutually independent random variables. Denote the probability density functions of $\{Y_i(\omega)\}_{i=1}^N$ as ρ_i, $i = 1,\ldots,N$. Let Γ_i be the image of Y_i. Then $\rho(\boldsymbol{Y}) = \prod_{i=1}^N \rho_i(Y_i)$ is the joint probability density of $\boldsymbol{Y} = (Y_1,\ldots,Y_N)$ with support $\Gamma \equiv \Gamma_1 \times \Gamma_2 \times \cdots \times \Gamma_N \in \mathbb{R}^N$. Then the stochastic log permeability can be represented by $G(\boldsymbol{x},\omega) = G(\boldsymbol{x},Y_1,\ldots,Y_N) = G(\boldsymbol{x},\boldsymbol{Y})$.

2.1. Stochastic variational formulation

By using the Doob–Dynkin lemma [43], the solutions of Eqs. (4) and (5) can be described by the same set of random variables $\{Y_i(\omega)\}_{i=1}^N$. Following [49], we define appropriate function spaces that encode variations of the function in the physical domain $\mathcal{D}$ and in the stochastic space Γ.

In the physical space, we introduce the following common functional spaces [17,49]:

$$W \equiv L^2(D) = \left\{ p : \int_D |p|^2 d\boldsymbol{x} = \|p\|^2_{L^2(D)} < +\infty \right\}, \tag{8}$$

with inner product

$$(p,q) \equiv (p,q)_{L^2(D)} := \int_D pq d\boldsymbol{x}, \quad p,q \in L^2(D), \tag{9}$$

and

$$H(\mathrm{div},D) = \{\boldsymbol{u} : \boldsymbol{u} \in (L^2(D))^2, \nabla\cdot\boldsymbol{u} \in L^2(D)\}, \tag{10}$$

with inner product

$$(\boldsymbol{u},\boldsymbol{v}) \equiv (\boldsymbol{u},\boldsymbol{v})_{H(\mathrm{div},D)} := \int_D \boldsymbol{u}\cdot\boldsymbol{v} \quad d\boldsymbol{x}, \boldsymbol{u},\boldsymbol{v} \in H(\mathrm{div},D). \tag{11}$$

We will also make use of the following space:

$$V \equiv H_{0,u}(\mathrm{div},D) = \{\boldsymbol{u} : \boldsymbol{u} \in H(\mathrm{div},D), \boldsymbol{u}\cdot\boldsymbol{n} = 0\}. \tag{12}$$

The duality product is defined as:

$$\langle \bar{u},\bar{p}\rangle \equiv \langle \bar{u},\bar{p}\rangle_{\partial D_p} := \int_{\partial D_p} \bar{u}\bar{p} dx, \quad \bar{u} \in H^{1/2}(D), \quad \bar{p} \in H^{-1/2}(D). \tag{13}$$

The functional space in Γ is defined as follows:

$$\mathcal{U} \equiv L^2_\rho(\Gamma) = \left\{ p : \left(\int_\Gamma |p(\boldsymbol{Y})|^2 \rho(\boldsymbol{Y}) d\boldsymbol{Y} \right)^{1/2} < \infty \right\}. \tag{14}$$

By taking its tensor product with the previous deterministic spaces, one can form the stochastic functional spaces:

$$\mathcal{W} = \mathcal{U}\otimes W, \quad \mathcal{V} = \mathcal{U}\otimes V. \tag{15}$$

Multiplication of Eqs. (4) and (5) by appropriate test functions and integration by parts leads to the following weak formulations: find $\boldsymbol{u} \in \mathcal{V}, p \in \mathcal{W}$ such that

$$\int_\Gamma (K^{-1}\boldsymbol{u}, \boldsymbol{v})\rho(\boldsymbol{Y})d\boldsymbol{Y} - \int_\Gamma (\nabla \cdot \boldsymbol{v}, p)\rho(\boldsymbol{Y})d\boldsymbol{Y} = -\int_\Gamma \langle \boldsymbol{v}\cdot\boldsymbol{n}, \bar{p}\rangle \rho(\boldsymbol{Y})d\boldsymbol{Y}, \quad \forall \boldsymbol{v} \in \mathcal{V}, \tag{16}$$

$$\int_\Gamma (l, \nabla \cdot \boldsymbol{u})\rho(\boldsymbol{Y})d\boldsymbol{Y} = 0, \quad \forall l \in \mathcal{W}, \tag{17}$$

and $S \in \mathcal{W}$ for each $t \in [0,T]$ such that

$$\int_\Gamma \left(\frac{\partial S}{\partial t}, q\right)\rho(\boldsymbol{Y})d\boldsymbol{Y} + \int_\Gamma (\boldsymbol{u}\cdot\nabla S, q)\rho(\boldsymbol{Y})d\boldsymbol{Y} = 0, \quad \forall q \in \mathcal{W}. \tag{18}$$

Without loss of generality, we assume that the support of the random variables Y_i is $\Gamma^i = [0,1]$ for $i = 1,\ldots,N$ and thus the bounded stochastic space is a N-hypercube $\Gamma = [0,1]^N$.

3. High dimensional model representation technique (HDMR) for the solution of SPDEs

The original infinite-dimensional stochastic problem is now restated as a finite N-dimensional problem. Then we can apply any stochastic method in the random space and the resulting equations become a set of deterministic equations in the physical space that can be solved by any standard deterministic discretization technique, e.g. the finite element method. The solution to the above SPDEs Eqs. (16)–(18) can be regarded as stochastic functions taking real values in the stochastic space Γ. For example, we can consider the pressure as a stochastic function $p : \Gamma \to \mathbb{R}$ and we use the notation $p(\boldsymbol{Y})$ to highlight the dependence on the randomness. Then it can be shown that the weak formulation Eqs. (16)–(18) is equivalent to [39]: for a.e. $\rho \in \Gamma$ the following deterministic weak form equations hold:

$$(K^{-1}\boldsymbol{u}, \boldsymbol{v}) - (p, \nabla\cdot\boldsymbol{v}) = -\langle \bar{p}, \boldsymbol{v}\cdot\boldsymbol{n}\rangle, \quad \forall \boldsymbol{v} \in V, \tag{19}$$

$$(l, \nabla\cdot\boldsymbol{u}) = 0, \quad \forall l \in W, \tag{20}$$

$$\left(\frac{\partial S}{\partial t}, q\right) + (q, \boldsymbol{u}\cdot\nabla S) = 0,, \quad \forall q \in W. \tag{21}$$

This nature is utilized by the stochastic collocation method, where the basic idea is to employ a finite element approximation for the spatial domain and approximate the multi-dimensional stochastic space Γ using interpolating functions on a set of collocation points $\{\boldsymbol{Y}_i\}_{i=1}^M \in \Gamma$ [43]. In the next section, a recent method HDMR is used to construct the multi-dimensional interpolant.

3.1. High dimensional model representation (HDMR)

In this section, the basic concepts of HDMR are briefly reviewed following closely the notation in [44]. For detailed descriptions of the ASGC and HDMR applied to stochastic systems, the interesting reader may refer to [43,44].

In order to alleviate the *curse of dimensionality*, we have combined ASGC with the adaptive stochastic high dimensional model representation (HDMR) technique in [44]. HDMR represents the model outputs as a finite hierarchical correlated function expansion in terms of the stochastic inputs starting from lower-order to higher-order component functions. In that work, the CUT-HDMR is adopted to construct the response surface of the stochastic solution. Within the framework of CUT-HDMR, a reference point $\overline{\boldsymbol{Y}} = (\overline{Y}_1, \overline{Y}_2, \ldots, \overline{Y}_N)$ is first chosen. According to our past experience, the mean vector of the random input $\boldsymbol{Y}$ is a good choice for the reference point. Then HDMR is given in a compact form as [44]

$$f(\boldsymbol{Y}) = \sum_{\mathbf{u}\subseteq\mathcal{D}}\sum_{\mathbf{v}\subseteq\mathbf{u}} (-1)^{|\mathbf{u}|-|\mathbf{v}|} f(\boldsymbol{Y}_{\mathbf{v}})|_{\boldsymbol{Y}=\overline{\boldsymbol{Y}}\setminus\boldsymbol{Y}_{\mathbf{v}}}, \tag{22}$$

for a given set $\mathbf{u} \subseteq \mathcal{D}$, where $\mathcal{D} := \{1,\ldots,N\}$ denotes the set of coordinate indices and we define $f(\boldsymbol{Y}_\emptyset) = f(\overline{\boldsymbol{Y}})$. Here, $\boldsymbol{Y}_{\mathbf{v}}$ denotes the $|\mathbf{v}|$-dimensional vector containing those components of $\boldsymbol{Y}$ whose indices belong to the set $\mathbf{v}$, where $|\mathbf{v}|$ is the cardinality of the corresponding set $\mathbf{v}$, i.e. $\boldsymbol{Y}_{\mathbf{v}} = (Y_i)_{i\in\mathbf{v}}$. The notation $\boldsymbol{Y} = \overline{\boldsymbol{Y}} \setminus \boldsymbol{Y}_{\mathbf{v}}$ means that the components of $\boldsymbol{Y}$ other than those indices that belong to the set $\mathbf{v}$ are set equal to those of the reference point. For example, if $\mathbf{v} = \{1, 3, 5\}$, then $|\mathbf{v}| = 3$ and $f(\boldsymbol{Y}_{\mathbf{v}})$ is a function of only three random variables Y_1, Y_3, Y_5 while the other dimensions satisfy $Y_i = \overline{Y}_i$ for $i \in \mathcal{D}$ and $i \notin \mathbf{v}$.

Therefore, the N-dimensional stochastic problem is transformed to several lower-order $|\mathbf{v}|$-dimensional problems $f(\boldsymbol{Y}_{\mathbf{v}})$ which can be easily solved by the ASGC [44]:

$$f(\boldsymbol{Y}) = \sum_{\mathbf{u}\subseteq\mathcal{D}}\sum_{\mathbf{v}\subseteq\mathbf{u}} (-1)^{|\mathbf{u}|-|\mathbf{v}|} \sum_{\|\mathbf{i}\|\leqslant N+r}\sum_{\mathbf{j}} w_{\mathbf{v}}^{\mathbf{ij}}(\boldsymbol{x})\cdot a_{\mathbf{j}}^{\mathbf{i}}(\boldsymbol{Y}_{\mathbf{v}}), \tag{23}$$

where the multi-index $\mathbf{i} = (i_1,\ldots,i_{|\mathbf{v}|}) \in \mathbb{N}^{|\mathbf{v}|}$, the multi-index $\mathbf{j} = (j_1,\ldots,j_{|\mathbf{v}|}) \in \mathbb{N}^{|\mathbf{v}|}$ and $\|\mathbf{i}\| = i_1 + \cdots + i_{|\mathbf{v}|}$. r is the sparse grid interpolation level and the summation for $\mathbf{j}$ is over collocation points selected in a hierarchical framework [43]. Here, $w_{\mathbf{v}}^{\mathbf{ij}}(\boldsymbol{x})$ is the hierarchical surplus for different sub-problems indexed by $\mathbf{v}$, which is just the difference between the function value at

the current point and interpolation value from the coarser grid. $a^{\mathbf{i}}_{\mathbf{j}}(\boldsymbol{Y}_{\mathbf{v}})$ is the multi-linear basis function constructed from the tensor product of the corresponding one-dimensional functions, which here is only a function of the coordinates belonging to the set $\mathbf{v}$.

In the context of incorporating adaptivity, we have chosen the collocation points based on the Newton–Cotes formulae using equidistant support nodes. The basic idea of adaptive sparse grid collocation (ASGC) method here is to use a chosen error indicator which incorporates the information from the hierarchical surplus to detect the smoothness of the solution and refine the hierarchical basis functions whose magnitude is equal or greater than ε, where ε is a predefined adaptive refinement threshold. If this criterion is satisfied, we simply add the $2N$ neighbor points to the current point of the sparse grid [43].

In addition, it is also easy to extract statistics by integrating directly the interpolating basis functions. The probability density function $\rho(\boldsymbol{Y})$ is 1 since the stochastic space is a unit hypercube $[0,1]^N$. As shown in [43], the multi-dimensional integral is simply the product of the 1D integrals which can be computed analytically. Denoting $\int_\Gamma a^{\mathbf{i}}_{\mathbf{j}}(\boldsymbol{Y})d\boldsymbol{Y} = l^{\mathbf{i}}_{\mathbf{j}}$, then we have

$$J_{\mathbf{u}} = \sum_{\mathbf{v}\subseteq\mathbf{u}}(-1)^{|\mathbf{u}|-|\mathbf{v}|}\sum_{\|\mathbf{i}\|\leqslant N+r}\sum_{\mathbf{j}} w^{\mathbf{ij}}_{\mathbf{v}}(\boldsymbol{x})\cdot l^{\mathbf{i}}_{\mathbf{j}}, \tag{24}$$

as the mean of the component function $f_{\mathbf{u}}$. Then the mean of the HDMR expansion is simply $\mathbb{E}[f(\boldsymbol{Y})] = \sum_{\mathbf{u}\subseteq\mathcal{D}} J_{\mathbf{u}}$. To obtain the variance of the solution, we can similarly construct an approximation for u^2 and use the formula $\mathrm{Var}[u(\boldsymbol{x})] = \mathbb{E}[u^2(\boldsymbol{x})] - (\mathbb{E}[u(\boldsymbol{x})])^2$.

It is noted that the solution method of each sub-problem is not limited to ASGC. It is also possible to use the sparse grid based on Gauss quadrature rule [40,42] to integrate the component functions of the CUT-HDMR in order to obtain the mean and the standard deviation directly. In this case, Eq. (24) can be rewritten as

$$J_{\mathbf{u}} = \sum_{\mathbf{v}\subseteq\mathbf{u}}(-1)^{|\mathbf{u}|-|\mathbf{v}|}\sum_{\|\mathbf{i}\|\leqslant N+r}\sum_{\mathbf{j}} \Omega^{\mathbf{ij}}_{\mathbf{v}}\cdot f(\boldsymbol{x}, \boldsymbol{Y}_{\mathbf{ij}}), \tag{25}$$

where Ω is the quadrature weight and $f(\boldsymbol{x},\boldsymbol{Y})$ is the function value at the collocation points. The advantage of this method is its higher accuracy than the linear interpolation. With Gauss quadrature, we can compute the mean and the standard deviation directly, however, we do not have a surrogate model (function approximation) like when using ASGC. In this work, we would also like to extend our previous ASGC formulation to include the Gauss quadrature rule.

As shown in [44], it is not necessary to compute all the terms in Eq. (22). We can take only a subset $\mathcal{S}$ of all indices $\mathbf{u}\subseteq\mathcal{D}$ while retaining the approximation accuracy. Therefore, we can define an interpolation formula $\mathcal{A}_{\mathcal{S}}f$ for the approximation of f which is given by

$$\mathcal{A}_{\mathcal{S}}f := \sum_{\mathbf{u}\in\mathcal{S}}\mathcal{A}(f_{\mathbf{u}}). \tag{26}$$

Here, $\mathcal{A}(f_{\mathbf{u}})$ is the sparse grid interpolant of the component function $f_{\mathbf{u}}$ and $\mathcal{A}_{\mathcal{S}}f$ is the interpolant of the function f using the proposed method with the index set $\mathcal{S}$. It is common to refer to the terms $\{f_{\mathbf{u}}: |\mathbf{u}| = m\}$ collectively as the "order-m terms". Then the expansion order for the decomposition Eq. (26) is defined as the maximum of m. Note that the number of collocation points in this expansion is defined as the sum of the number of points for each sub-problem from Eq. (23), i.e. $M = \sum_{\mathbf{u}\in\mathcal{S}} M_{\mathbf{u}}$.

Based on this, we have also developed the adaptive version of HDMR to find the optimal set $\mathcal{S}$ in [44]. A weight is defined for each expansion term in [44]. We always construct the zeroth- and first-order HDMR expansion to identify the important dimensions if the weight is greater than a predefined error threshold θ_1. Then we adaptively construct higher-order component functions increasingly from lower-order to higher-order and again only select those terms whose weight is greater than θ_1. In this way, we find those terms which may have significant contribution to the overall expansion while ignoring other trivial terms thus reducing the computational cost for high-dimensional problems. In addition, if the relative error between two consecutive orders is smaller than another threshold θ_2, the HDMR expansion is considered converged and the construction stops. For more details, please refer to [44].

4. Spatial finite element discretization

As stated in Section 3, in order to utilize the HDMR Eq. (23), we only need to seek the solution $(\boldsymbol{u}, p, S)$ at each collocation point in the stochastic space Γ. In other words, our goal is reduced to: for each permeability realization $K^{(i)}(\boldsymbol{x}) = K(\boldsymbol{x}, \boldsymbol{Y}_i)$, $i = 1,\ldots,M$, we solve the deterministic problem: find $\boldsymbol{u}^{(i)}\in V$, $p^{(i)}\in W$ and $S^{(i)}\in W$ such that for $i = 1,\ldots,M$

$$(K^{-1}\boldsymbol{u}^{(i)}, \boldsymbol{v}) - (p^{(i)}, \nabla\cdot\boldsymbol{v}) = -\langle\bar{p}, \boldsymbol{v}\cdot\boldsymbol{n}\rangle, \quad \forall\boldsymbol{v}\in V, \tag{27}$$

$$(l, \nabla\cdot\boldsymbol{u}^{(i)}) = 0, \quad \forall l\in W, \tag{28}$$

$$\left(\frac{\partial S^{(i)}}{\partial t}, q\right) + (q, \boldsymbol{u}^{(i)}\cdot\nabla S^{(i)}) = 0, \quad \forall q\in W. \tag{29}$$

In this section, mixed finite element methods are introduced to solve the above equations in the spatial domain. Since the pressure Eqs. (27) and (28) are effectively decoupled from the saturation equation (29), we will first introduce the multiscale

method to find $\boldsymbol{u}$, p and then use the upwinding finite element method to find S. To simplify the notation, we will omit the superscript i and assume the deterministic equations are satisfied for an arbitrary permeability sample in the stochastic space.

4.1. Mixed finite element heterogeneous multiscale method (MxHMM)

In the porous media flow problem, the heterogeneity of the permeability field will have a great impact on the global flow conditions. In order to resolve the fine-scale velocity accurately with lower computational cost, a multiscale method is needed. In addition, the mixed finite element method is also required to compute the velocity and pressure simultaneously, if we want to have an accurate velocity and ensure mass conservation. We can identify at least two main multiscale methods: multiscale finite element or finite volume methods [8,10,12] and the variational multiscale methods [15,17]. In this section, we will develop a multiscale method which is based on the framework of the heterogeneous multiscale method [23]. We present the discretization and methodology for a two-dimensional system. Extension to three-dimensions is straightforward.

Consider a partition, $\mathcal{T}_h$ for the domain D into non-overlapping elements $e_i, \mathcal{T}_h = \bigcup_{i=1}^{N_h} e_i$, where N_h is the number of elements of the grid. Define also the skeleton of the partition, $\mathcal{SP}_h = \bigcup_{a=1}^{M_h} v_a$, where M_h is the number of element faces denoted by v_a. The partition $\mathcal{T}_h$ is regarded as the fine-scale grid. The multiscale permeability is defined as a cell-wise constant on this grid. To implement the multiscale method, we also consider a coarse-scale partition of the same domain D. Denote this partition as $\mathcal{T}_c = \bigcup_{i=1}^{N_c} E_i$. Denote by $\mathcal{SP}_c = \bigcup_{a=1}^{M_c} \Lambda_a$ the associated skeleton of the coarse-scale discretization. Here, N_c is the number of coarse elements and M_c is the number of coarse element faces denoted by Λ_a. In order to conserve the mass at the coarse-scale, we also assume for simplicity that the partitions $\mathcal{T}_h$ and $\mathcal{T}_c$ are nested, conforming and consist of rectangular elements. Fig. 1 shows a fine grid (finer lines) and a corresponding coarse grid (heavier lines).

4.1.1. The coarse-scale mixed finite element discretization

Now consider the finite dimensional subspaces on the coarse-scale $V_c \in V$ and $W_c \in W$. The mixed finite element method approximation of Eqs. (27) and (28) on the coarse-scale reads: find the coarse-scale $(\boldsymbol{u}_c, p_c) \in V_c \times W_c$ such that

$$(K^{-1}\boldsymbol{u}_c, \boldsymbol{v}_c) - (p_c, \nabla \cdot \boldsymbol{v}_c) = -\langle \bar{p}, \boldsymbol{v}_c \cdot \boldsymbol{n} \rangle, \quad \forall \boldsymbol{v}_c \in V_c, \tag{30}$$

$$(l_c, \nabla \cdot \boldsymbol{u}_c) = 0, \quad \forall l_c \in W_c. \tag{31}$$

Note that V_c and W_c should satisfy the discrete inf–sup condition [55]. In this work, V_c is taken to be the lowest-order Raviart–Thomas space [9], $RT_0(\mathcal{T}_c)$ and W_c is taken to be the space of piece-wise constants on the coarse-scale mesh, $P_0(\mathcal{T}_c)$. Other choices can be found in [55]. Therefore, we define the finite element space for the coarse-scale velocity as:

$$V_c = \left\{ \boldsymbol{u}_c : \boldsymbol{u}_c = \sum_{a=1}^{M_c} \boldsymbol{\psi}_a^c u_a^c, \quad u_a^c = 0, \quad \forall \Lambda_a \in \partial D_u \right\}, \tag{32}$$

where $\boldsymbol{\psi}_a^c$ is the RT_0 basis functions on the uniform mesh of rectangular elements associated with the coarse element face Λ_a. For a reference element $E = [x_1^L, x_1^R] \times [x_2^L, x_2^R]$ with the area $|E|$, there are four vector RT_0 basis functions with non-zero support:

$$\boldsymbol{\psi}_1^c = \left[(x_1^R - x_1)/(x_1^R - x_1^L), 0 \right]^T, \quad \boldsymbol{\psi}_2^c = \left[0, (x_2^R - x_2)/(x_2^R - x_2^L) \right]^T, \tag{33}$$

$$\boldsymbol{\psi}_3^c = \left[(x_1 - x_1^L)/(x_1^R - x_1^L), 0 \right]^T, \quad \boldsymbol{\psi}_4^c = \left[0, (x_2 - x_2^L)/(x_2^R - x_2^L) \right]^T. \tag{34}$$

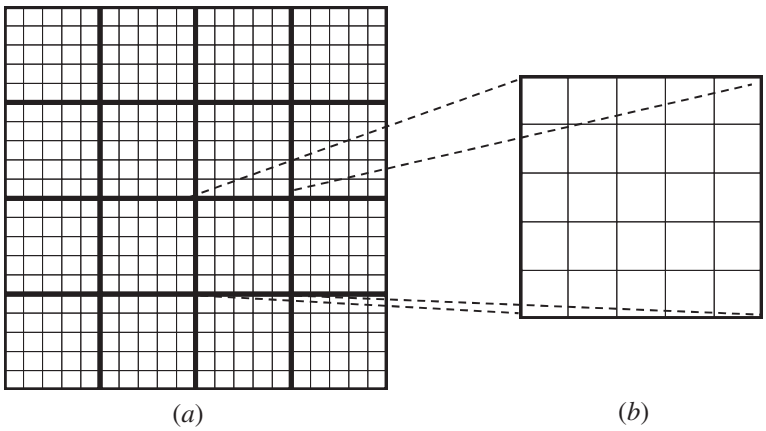

Fig. 1. Schematic of the domain partition: (a) fine- and coarse-scale grids and (b) fine-scale local region in one coarse element.

The basis functions satisfy the properties such that $\psi_i^c \cdot \boldsymbol{n}_j = 1$ if $i = j$, otherwise $\psi_i^c \cdot \boldsymbol{n}_j = 0$ for $i, j = 1,\ldots,4$. Therefore u_a^c is value of the coarse-scale flux at the middle point of the side Λ_a, i.e. $\boldsymbol{u}_c \cdot \boldsymbol{n}_a = u_a^c$, where $\boldsymbol{n}_a$ is the unit outer normal to the interface Λ_a. The coarse-scale pressure approximation is piecewise constant on the coarse-mesh and $P_0(\mathcal{T}_c)$ is

$$W_c = \left\{ p_c : p_c = \sum_{a=1}^{N_c} \phi_i^c p_i^c \right\}, \tag{35}$$

where ϕ_i^c is the coarse-scale pressure basis function for the coarse element i defined as

$$\phi_i^c(\boldsymbol{x}) = \begin{cases} 1, & \text{if } \boldsymbol{x} \in E_i, \\ 0, & \text{if } \boldsymbol{x} \notin E_i. \end{cases} \tag{36}$$

p_i^c is the corresponding pressure degree of freedom (the average pressure in coarse element E_i).

4.1.2. The modified bilinear form and the subgrid problem

From the mixed finite element formulation of Eqs. (30) and (31), we can assemble the global linear system of equations. It is noted that only the bilinear form $(K^{-1}\boldsymbol{u}_c, \boldsymbol{v}_c)$ has the contribution from the fine-scale permeability. Denote $A = (A_{ij})$ the global matrix from assembling the bilinear form $(K^{-1}\boldsymbol{u}_c, \boldsymbol{v}_c)$, where

$$A_{ij} = \int_D \psi_i^c(\boldsymbol{x}) \cdot K^{-1}(\boldsymbol{x}) \psi_j^c(\boldsymbol{x}) d\boldsymbol{x}. \tag{37}$$

We could evaluate Eq. (37) by the 2×2 Gauss quadrature rule in each coarse element: let

$$f_{ij}(\boldsymbol{x}) = \psi_i^c(\boldsymbol{x}) \cdot K^{-1}(\boldsymbol{x}) \psi_j^c(\boldsymbol{x}), \tag{38}$$

then

$$A_{ij} = \int_D f_{ij} d\boldsymbol{x} \simeq \sum_{E \in \mathcal{T}_c} \sum_{\xi_k \in E} \tau_k f_{ij}(\xi_k), \tag{39}$$

where ξ_k and τ_k, $k = 1,\ldots,4$ are the quadrature points and weights (including the determinant of the Jacobian matrix) in the coarse element E, respectively.

It is obvious that any realization of the permeability field at the quadrature point $K(\xi_k)$ is not able to capture the full information at the subgrid scale in the corresponding coarse element since the size of the coarse element is much larger than the characteristic length scale of the multiscale permeability field. Therefore, following the framework of the heterogeneous multiscale method [22,27], in order to capture more information from subgrid scale, we need to modify the bilinear form Eq. (38) at the quadrature point ξ_k as:

$$f_{ij}(\xi_k) = \frac{1}{|E_{\delta_k}|} \int_{E_{\delta_k}} \tilde{\boldsymbol{u}}_{ik}(\boldsymbol{x}) \cdot K^{-1} \tilde{\boldsymbol{u}}_{jk}(\boldsymbol{x}) d\boldsymbol{x}, \quad k = 1,\ldots,4, \tag{40}$$

where $\tilde{\boldsymbol{u}}_{ik}(\boldsymbol{x})$, $i = 1,\ldots,4$ is the solution to the following local subgrid problem in each sampling domain $E_{\delta_k} \subset E$, $k = 1,\ldots,4$:

$$\nabla \cdot \tilde{\boldsymbol{u}}_{ik}(\boldsymbol{x}) = 0, \quad \tilde{\boldsymbol{u}}_{ik}(\boldsymbol{x}) = -K \nabla \tilde{p}_{ik}(\boldsymbol{x}), \quad \forall \boldsymbol{x} \in E_{\delta_k}, \tag{41}$$

with appropriate boundary conditions which we will discuss later. $\tilde{p}_i(\boldsymbol{x})$ can be considered as the subgrid pressure.

4.1.3. The choice of the sample domain E_{δ_k}

First, we will discuss the choice of the sampling domain E_{δ_k} of the subgrid problem. In the original problem definition of the FeHMM [22,27], the coefficient of the elliptic equation (here K) is assumed to be periodic. Therefore, the sampling domain was taken around each quadrature point as $E_{\delta_k} = \xi_k + \delta I$, where $I = (-1/2, 1/2)^2$ and δ is equal to one period of the coefficient in the elliptic equation, as in Fig. 2(a).

However, in general, the permeability is not periodic. If the sampling domain is too small, one cannot capture enough information on the subgrid scale. According to the numerical results in [1,3,8,11,56,57], the larger the size of the sampling domain is, the more accurate the computed result is. Therefore, we would like to take the sampling domain to be the same as the coarse element, i.e. $E_{\delta_k} = E$, $\partial E_{\delta_k} = \partial E$ as in Fig. 2(b). In addition, we also assume that the fine grid within each coarse element is the same as the fine-scale grid $\mathcal{T}_h$, where the permeability is defined, see Fig. 1(b). In this way, we can ensure global continuity of the flux across the coarse element.

4.1.4. The choice of the boundary conditions

Hence, all the subgrid problems are solved within the same coarse element. The only difference is the applied boundary condition. The boundary condition of the problem in Eq. (41) plays a significant role in the accuracy of the multiscale method as discussed in [56], where three different boundary conditions are considered: the periodic boundary condition, Dirichlet boundary condition, and the Neumann boundary condition. However, when mixed finite element formulation is used on

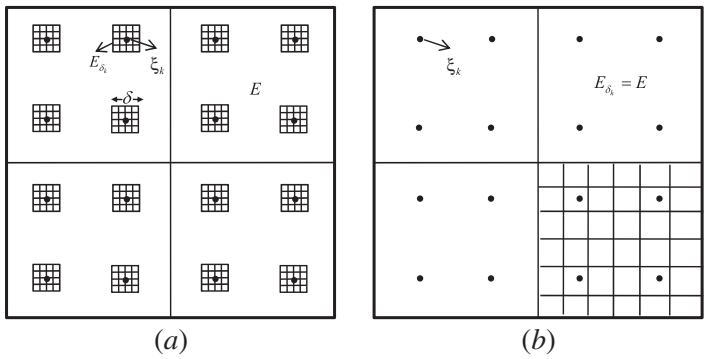

Fig. 2. (a) Schematic of the original HMM method, where the sampling domain is around the quadrature point. (b) Schematic of the proposed MxHMM method, where the sampling domain is the same as the coarse element.

the coarse-scale, only the Neumann boundary condition is applicable here. In [27], the following Neumann boundary condition is proposed:

$$\tilde{\boldsymbol{u}}_{ik} \cdot \boldsymbol{n}_{\partial E} = \boldsymbol{\psi}_i^c(\boldsymbol{\xi}_k) \cdot \boldsymbol{n}_{\partial E}, \text{ on } \partial E, \tag{42}$$

where $\boldsymbol{\psi}_i^c(\boldsymbol{\xi}_k)$ denotes the value of the ith coarse-scale RT_0 finite element basis function at the quadrature point $\boldsymbol{\xi}_k$, $k = 1,\ldots,4$ and $\boldsymbol{n}_{\partial E}$ denotes the unit outer normal of the coarse element boundary ∂E. According to the definition of RT_0 basis function in Eqs. (33) and (34), this boundary condition applies a uniform flow with magnitude $\boldsymbol{\psi}_i^c(\boldsymbol{\xi}_k)$ from one side to the opposite side while keeping no-flow conditions on the other two sides. The example of $\boldsymbol{\psi}_1(\xi_1)$ is shown in Fig. 3. However, this boundary condition only reflects the local heterogeneity structure within the current coarse element. It does not contain the flow condition across the coarse element interface which is often important in guaranteeing the continuity of flux on the coarse-scale. Therefore, we would like to propose a new boundary condition which reflects the heterogeneous structure across the coarse element boundary.

For a fine-scale element interface v_a, denote the two adjacent fine-scale elements as e_i and e_j, i.e. $v_a = e_i \bigcap e_j$. According to two-point flux approximation finite volume method, if the element interface is in the y-direction, the element interface transmissibility in the x-dimension is defined by Gautier et al. [58]:

$$T_{v_a} = 2|v_a|\left(\frac{\Delta x_i}{K_i} + \frac{\Delta x_j}{K_j}\right)^{-1}, \tag{43}$$

where $|v_a|$ is the length of the interface, Δx_i denote the length of element e_i in the x-coordinate direction, and K_i is the permeability in element e_i. Similar expression can be defined in the y-dimension. The fine-scale transmissibility of interface v_a reflects the flow condition across elements. Denote the total applied flux along the coarse element interface Λ due to the value of the ith coarse-scale basis functions at the kth quadrature point as

$$Q_{ik} = \int_\Lambda \boldsymbol{\psi}_i^c(\boldsymbol{\xi}_k) \cdot \boldsymbol{n}\, ds = |\Lambda| \boldsymbol{\psi}_i^c(\boldsymbol{\xi}_k) \cdot \boldsymbol{n}_\Lambda. \tag{44}$$

In this work, we consider rectangular elements oriented along the coordinate axes. Hence, we modify the boundary condition Eq. (42) to:

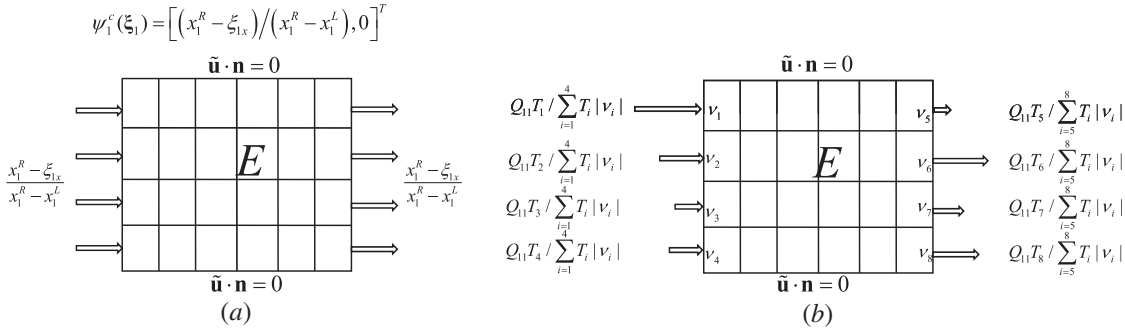

Fig. 3. Schematic of different boundary conditions. (a) The uniform boundary condition. (b) The modified boundary condition where the flux is scaled according to the fine-scale transmissibilities.

$$\tilde{\boldsymbol{u}}_{ik}\cdot\boldsymbol{n}|_{\Lambda}=Q_{ik}\cdot\frac{T_{v_a}}{\sum_{v_b\subset\Lambda}T_{v_b}|v_b|},\quad \text{on } \Lambda\subset\partial E, \tag{45}$$

where Q_{ik} is defined in Eq. (44) and T_{v_a} is the fine-scale transmissibility of interface $v_a\subset\Lambda$ as defined in Eq. (43) for an interface in the y-direction. See for example Q_{11} in Fig. 3(b). When the interface is in the x-direction, we change the definition of T_{v_a} accordingly. It is clear that the sum of the flux applied on the fine-scale element from Eq. (42) is equal to the total flux applied on the same coarse element boundary from Eq. (45). In other words, we just redistribute the total flux on the coarse-scale element boundary according to the ability to transport the flow at the interface of each fine-scale element. This is clearly a better choice for boundary condition since it reflects the flow conditions across the inter-block boundaries.

4.1.5. Final coarse-scale and subgrid scale problems

Finally, our subgrid problem in a coarse-element E is defined as follows: For each quadrature point ξ_k, $k=1,\ldots,4$, we seek the solution $\tilde{\boldsymbol{u}}_{ik}$ to the following subgrid problem for each coarse-scale RT_0 basis function $\boldsymbol{\psi}_i^c,\ i=1,\ldots,4$:

$$\nabla\tilde{\boldsymbol{u}}_{ik}(\boldsymbol{x})=0,\quad \tilde{\boldsymbol{u}}_{ik}(\boldsymbol{x})=-K\nabla\tilde{p}_{ik}(\boldsymbol{x}),\quad \forall\,\boldsymbol{x}\in E, \tag{46}$$

with the Neumann boundary condition defined in Eq. (45).

For convenience, we will define the corresponding modified bilinear form as: for any $\boldsymbol{u}_c,\boldsymbol{v}_c\in V_c$

$$A_h(K^{-1}\boldsymbol{u}_c,\boldsymbol{v}_c):=\sum_{E\in\mathcal{T}_c}\sum_{k=1}^{4}\frac{\tau_k}{|E|}\int_E\boldsymbol{U}_k(\boldsymbol{x})\cdot K^{-1}\boldsymbol{V}_k(\boldsymbol{x})d\boldsymbol{x}, \tag{47}$$

where $\boldsymbol{U}$ and $\boldsymbol{V}$ are defined through the subgrid problems. The assembly of this bilinear form will be detailed in Section 4.1.6. Therefore, the MxHMM version of Eqs. (30) and (31) on the coarse-scale reads: Find the coarse-scale $(\boldsymbol{u}_c,p_c)\in V_c\times W_c$ such that

$$A_h(K^{-1}\boldsymbol{u}_c,\boldsymbol{v}_c)-(p_c,\nabla\cdot\boldsymbol{v}_c)=-\langle\bar{p},\boldsymbol{v}_c\cdot\boldsymbol{n}\rangle,\quad \forall\boldsymbol{v}_c\in V_c, \tag{48}$$

$$(l_c,\nabla\cdot\boldsymbol{u}_c)=0,\quad \forall l_c\in W_c, \tag{49}$$

with the boundary condition

$$p_c=\bar{p}\ \text{on}\ \partial D_p,\quad \boldsymbol{u}_c\cdot\boldsymbol{n}=0\ \text{on}\ \partial D_u. \tag{50}$$

The major difference between Eqs. (30),(31) and (48),(49) lies in the bilinear form $A_h(\cdot,\cdot)$, which needs solution of the local subgrid problem Eq. (46). It is through these subgrid problems and the mixed formulation that the effect of the heterogeneity on coarse-scale solutions can be correctly captured. Unfortunately, it is not trivial to analyze this multiscale method in a general case, but convergence results have been obtained using the homogenization theory in the case of periodic coefficients [27].

4.1.6. Solution of the subgrid problems and assembly of the bilinear form

In general, the subgrid problem Eq. (46) can be solved through the standard or mixed finite element method. In the present setting, since we are only interested in the velocity, the mixed finite element method is preferred. Let $E_h=\mathcal{T}_h(E)$ denote the fine grid defined over one coarse element E. As mentioned before, it coincides with the fine-scale grid $\mathcal{T}_h$. The subgrid-scale velocity functional spaces will be defined on the fine grid E_h of each coarse element:

$$V_E=\left\{\tilde{\boldsymbol{u}}:\tilde{\boldsymbol{u}}=\sum_{a=1}^{M_E}\boldsymbol{\psi}_a^h\tilde{u}_a^h,\quad \boldsymbol{\psi}_a^h\in RT_0(E_h)\right\}, \tag{51}$$

where M_E is the number of edges in E, and the pressure space is defined similarly:

$$W_E=\left\{\tilde{p}:\tilde{p}=\sum_{a=1}^{N_E}\phi_i^h\tilde{p}_i^h,\quad \phi_i^h\in P_0(E_h)\right\}, \tag{52}$$

where N_E is the number of elements in E. It is noted that, as the Neumann boundary conditions in Eq. (45) are imposed on all boundaries of the coarse element E, an extra constraint must be added to make the subgrid problem well posed. In our implementation, the pressure is prescribed to 0 at one of the elements in E_h.

The mixed finite element method approximation of Eq. (46) in coarse element E_i on the subgrid-scale grid reads: find the subgrid-scale $(\tilde{\boldsymbol{u}},\tilde{p})\in V_{E_i}\times W_{E_i}$ such that

$$(K^{-1}\tilde{\boldsymbol{u}},\tilde{\boldsymbol{v}})-(\tilde{p},\nabla\cdot\tilde{\boldsymbol{v}})=0,\quad \forall\tilde{\boldsymbol{v}}\in V_{E_i}, \tag{53}$$

$$(\tilde{l},\nabla\cdot\tilde{\boldsymbol{v}})=0,\quad \forall\tilde{l}\in W_{E_i}, \tag{54}$$

with the boundary condition Eq. (45). It is noted that for each coarse element, we need to solve 4 (number of quadrature points) $\times$ 4 (number of basis functions) = 16 subgrid problems. However, the only difference between them are in the boundary conditions. Therefore, we only need to assemble the stiffness matrix once and solve the same algebraic problem with different right hand vectors.

Following a standard assembly process for the global matrix of the coarse-scale bilinear form Eq. (47), we compute the contribution A_E to the global matrix associated with the coarse element E, where A_E is a 4×4 matrix. Assume the solution of the subgrid problem at the kth Gaussian point can be written as $\tilde{\boldsymbol{u}}_{ik} = \sum_{j=1}^{M_E} c_{ij}^k \boldsymbol{\psi}_j^h,\ i = 1, \ldots, 4$. We can write all the solutions as a $4 \times N_E$ matrix, $C_k = \left(c_{ij}^k\right)$ where the ith row contains the subgrid solution corresponding to the ith coarse-scale basis function ψ_i^c. Therefore, the value of A_E from the kth Gauss point can be denoted as $A_E^k = \left(a_E^k\right)_{ij}$, where

$$\left(a_E^k\right)_{ij} = \frac{\tau_k}{|E|} c_{il} \int_E K^{-1} \boldsymbol{\psi}_l^h \cdot \boldsymbol{\psi}_m^h d\boldsymbol{x}\ c_{jm}. \tag{55}$$

Denoting the bilinear form matrix from the subgrid-scale problem as $B^k = \left(b_{lm}^k\right),\ b_{lm}^k = \int_E K^{-1} \boldsymbol{\psi}_l^h \cdot \boldsymbol{\psi}_m^h d\boldsymbol{x}$, we can write:

$$A_E = \sum_{k=1}^{4} \frac{\tau_k}{|E|} C_k B^k (C_k)^T. \tag{56}$$

Finally, we would like to comment on the solution of the linear systems resulting from the mixed finite element discretization. The linear system is indefinite, and it is difficult to solve using a common iterative method. In our implementation, we use the Schur complement matrix to solve the pressure first and then solve the velocity [11]. The linear system is solved using preconditioned conjugate gradient method. All the implementations are based on the data structure of the numerical library PETSc [59].

4.2. Reconstruction of the fine-scale velocity and solution of transport equation

So far we have described the development of the mixed finite element heterogeneous multiscale method for the solution of the coarse-scale velocity. However, in order to simulate the transport equation accurately, we need to reconstruct the fine-scale velocity using the coarse-scale velocity and the subgrid permeability. It is noted that the coarse-scale velocity is not conservative at the fine-scale. In order to obtain a mass-conservative fine-scale velocity, we solve Darcy's equation within each coarse element E using Neumann boundary condition given by the coarse-scale flux along the coarse-element boundary. The coarse-scale flux, denoted by Q^c is directly given as the solution of the system of linear equations from the coarse-scale discretization. That is, for each $E \in \mathcal{T}_c$, one solves the fine-scale velocity $\boldsymbol{u}_h$ inside E by [18,58]

$$\nabla \cdot \boldsymbol{u}_h = 0, \quad \boldsymbol{u}_h = -K \nabla p_h, \quad \forall \boldsymbol{x} \in E, \tag{57}$$

with the boundary condition similar to the one used in Eq. (45):

$$\boldsymbol{u}_h \cdot \boldsymbol{n}|_{\Lambda} = Q^c \cdot \frac{T_{v_a}}{\sum_{v_b \subset \Lambda} T_{v_b} |v_b|},\ \text{on}\ \Lambda \subset \partial E, \tag{58}$$

where $Q^c = \int_{\Lambda} \boldsymbol{u}_c \cdot \boldsymbol{n} ds$ is the coarse-scale flux across the coarse element interface Λ, and T_{v_a} is the fine-scale transmissibility of interface $v_a \subset \Lambda$. Since $\boldsymbol{u}_c$ is the solution of the coarse-scale problem using the mixed finite element method, the coarse-scale flux Q^c is obtained directly. Similar to the subgrid problem, Neumann boundary condition is applied on all the boundaries of the coarse element. To obtain a unique solution of the above problem, the pressure is fixed to the coarse-scale pressure p_c in the center element of the mesh E_h. As indicated in [18,58,60], this reconstruction step guarantees the continuity of the flux across the fine-scale elements between two coarse blocks and accounts for subgrid heterogeneity. It also forces the sum of the fine grid fluxes to be equal to the corresponding coarse-scale flux. In this way, the resulting fine-scale velocity is conservative on fine-scale grid as well as the coarse-scale grid.

For the solution of the saturation equation, we use the upwinding finite element method [8,52], which is equivalent to the standard upstream weighted finite volume method. We also approximate the saturation as a piecewise constant in each fine-scale element e, $P_0(\mathcal{T}_h)$, the same as the pressure space. Given the discrete reconstructed fine-scale velocity field $\boldsymbol{u}_h$, for a fine-scale element $e \in \mathcal{T}_h$. We define the inflow boundary of the element as ∂e_-, if $\boldsymbol{u}_h \cdot \boldsymbol{n} < 0$ on ∂e_- and similarly the outflow boundary as ∂e_+, if $\boldsymbol{u}_h \cdot \boldsymbol{n} \geqslant 0$ on ∂e_+. For any piecewise constant function S_h over the mesh $\mathcal{T}_h$, the upwinding value on ∂e is defined as $\widetilde{S}_h$ and is equal to the interior trace of S_h if on ∂e_+ and equal to the exterior trace of S_h if on ∂e_-. In addition, we also assume $\widetilde{S}_h = 0$ on $\partial e_- \bigcap \partial D$.

Therefore, the weak formulation of the upwinding scheme is to find $S_h \in W_h$ such that

$$\int_D \frac{\partial S_h}{\partial t} q_h d\boldsymbol{x} + \sum_{e \in \mathcal{T}_h} \int_{\partial e} (\boldsymbol{u}_h \cdot \boldsymbol{n}) \widetilde{S}_h q_h ds = 0, \quad \forall q_h \in W_h. \tag{59}$$

Let Δt be the time step and denote by S_i^k the approximation of the water saturation in fine-scale element e_i at time t^k. Then the discrete form of the saturation Eq. (59) is:

$$S_i^{k+1} + \frac{\Delta t}{|e_i|} \sum_{j \neq i} f_{ij}\left(S^{k+1}\right) q_{ij} = S_i^k. \tag{60}$$

Here, $|e_i|$ is the area of the element e_i. $f_{ij}(S) = \max\{\text{sign}\,(q_{ij}) S_i, -\text{sign}\,(q_{ij}) S_j\}$ is the upwinding water saturation for the interface $v_{ij} = \partial e_i \bigcap \partial e_j$. Finally, the flux across the boundary is $q_{ij} = \int_{v_{ij}} \boldsymbol{u}_h \cdot \boldsymbol{n}_{ij} ds$ where $\boldsymbol{n}_{ij}$ is the unit normal to v_{ij} pointing from e_i to e_j.

It is noted that in Eq. (60), only the flux q_{ij} on the each interface is required. This value is directly computed as the solution from our multiscale approach. This is the main reason why the method discussed here is better than the stabilized conforming finite element method [61].

It is emphasized again that we consider the transport problem with unit mobility ratio, so the saturation changes will not affect the pressure or velocity. Therefore, we can first compute the fine-scale velocity with our multiscale approach and then solve the transport equation. The flow rate of produced oil at the outlet boundary is denotes as q_o and the flow rate of produced water q_w. To assess the quality of our multiscale approach, we will use the so called water cut curve F, which defines the fraction of water in the produced fluid, i.e., $F = q_w/(q_w + q_o)$ as a function of time measured in pore volume injected (PVI). The water-cut is defined as

$$F(t) = \frac{\int_{\partial D^{\text{out}}} (\boldsymbol{u}_h \cdot \boldsymbol{n}) S ds}{\int_{\partial D^{\text{out}}} (\boldsymbol{u}_h \cdot \boldsymbol{n}) ds}, \tag{61}$$

where ∂D^{out} refers to the part of the boundary with outer flow, i.e. $\boldsymbol{u}_h \cdot \boldsymbol{n} > 0$. PVI represents dimensionless time and is computed as

$$\text{PVI} = \int Q dt / V_p, \tag{62}$$

where V_p is the total pore volume of the system, which is equal to the area of the domain D here and $Q = \int_{\partial D^{\text{out}}} (\boldsymbol{u}_h \cdot \boldsymbol{n}) ds$ is the total flow rate.

The complete schematic of the stochastic multiscale method for porous media flow is illustrated in Fig. 4.

5. Numerical examples

In the first two examples, we solve the problem with deterministic permeability in order to validate the newly developed multiscale method. In the third example, the complete stochastic problem with a known covariance function is addressed.

5.1. Simulation in realistic two-dimensional reservoirs

This test case is a two-dimensional problem with a highly heterogeneous permeability. The permeability field shown in Fig. 5 is taken from the top layer of the 10-th SPE comparative solution project [62]. The fine grid on which the permeability is defined consists of 60×220 gridblocks. It has Dirichlet boundary conditions $\bar{p} = 100$ on $\{x_2 = 0\}$, $df\bar{p} = 0$ on $\{x_2 = 220\}$ and Neumann boundary conditions $\boldsymbol{u} \cdot \boldsymbol{n} = 0$ on both $\{x_1 = 0\}$, $\{x_1 = 60\}$. We also impose zero initial condition for saturation $S(x, 0) = 0$ and boundary condition $S(x, t) = 1$ on $\{x_2 = 0\}$.

The reference solution is computed on the fine-scale grid using single-scale mixed finite element method directly, as shown in Figs. 6(a) and 7(a). We also show the solutions obtained with the MxHMM method on various coarse grids in Figs. 6 and 7. It is seen that the flow focuses along the region with higher permeability while bypassing the low-permeability areas. At the same time, the velocity field displays significant small-scale structure corresponding to the spatial permeability variations. The multiscale solution successfully captures all the main characters of the fine-scale results and compares very

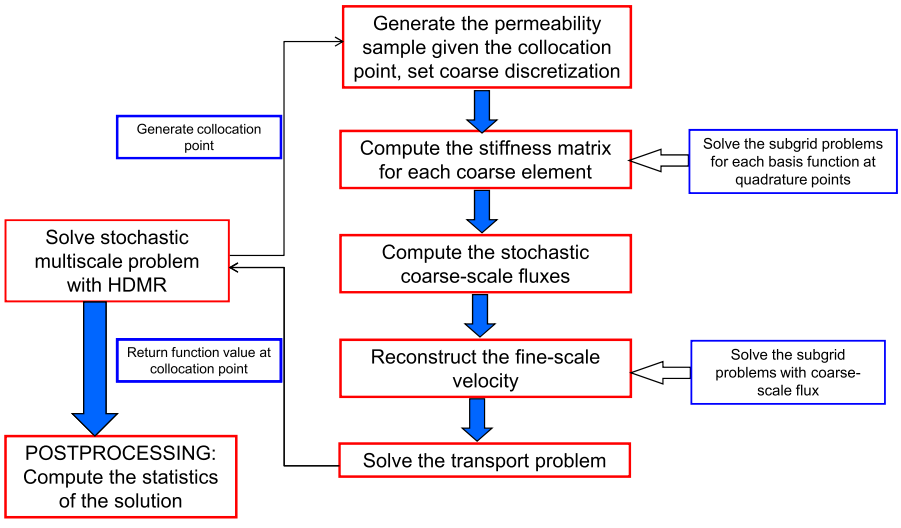

Fig. 4. Schematic of the developed stochastic multiscale method for porous media flow.

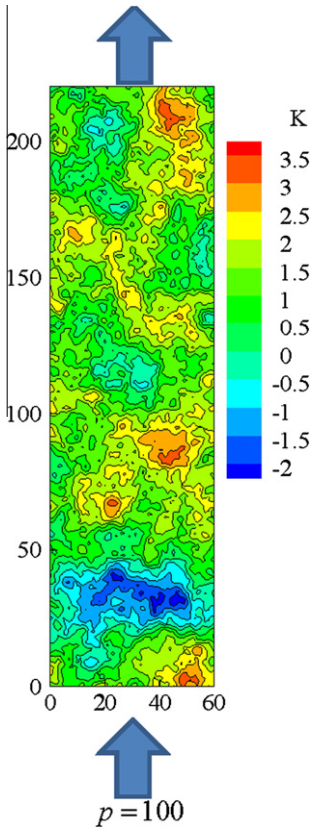

Fig. 5. Logarithm of the permeability field from the top layer of the 10th SPE model, which is defined on 60×220 fine grid.

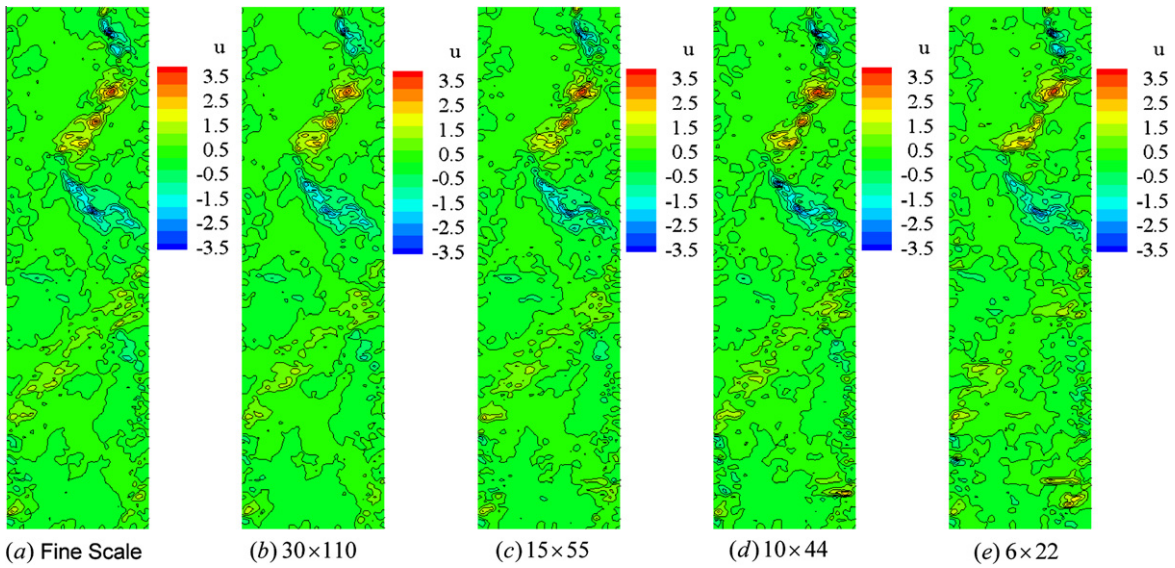

Fig. 6. Contour plots of the x-velocity component for various meshes: (a) 60×220 fine-scale grid, (b) 30×110 coarse grid, (c) 15×55 coarse grid, (d) 10×44 coarse grid, and (e) 6×22 coarse grid.

well with the fine-scale solution, with the two results being quite difficult to distinguish visually. As a direct measure of the error in the computed velocity field, we consider the L^2-norm: $\|\boldsymbol{u}\|_2 = (\int_D \boldsymbol{u} \cdot \boldsymbol{u} d\boldsymbol{x})^{1/2}$, where the corresponding relative error is given as $\delta(\boldsymbol{u}) = \|\boldsymbol{u}_{\text{ref}} - \boldsymbol{u}_{\text{ms}}\| / \|\boldsymbol{u}_{\text{ref}}\|$. The result is given in Table 1. In general, the error is larger with coarser grid which is possibly due to some large local error in the high permeability region where the velocity changes quickly.

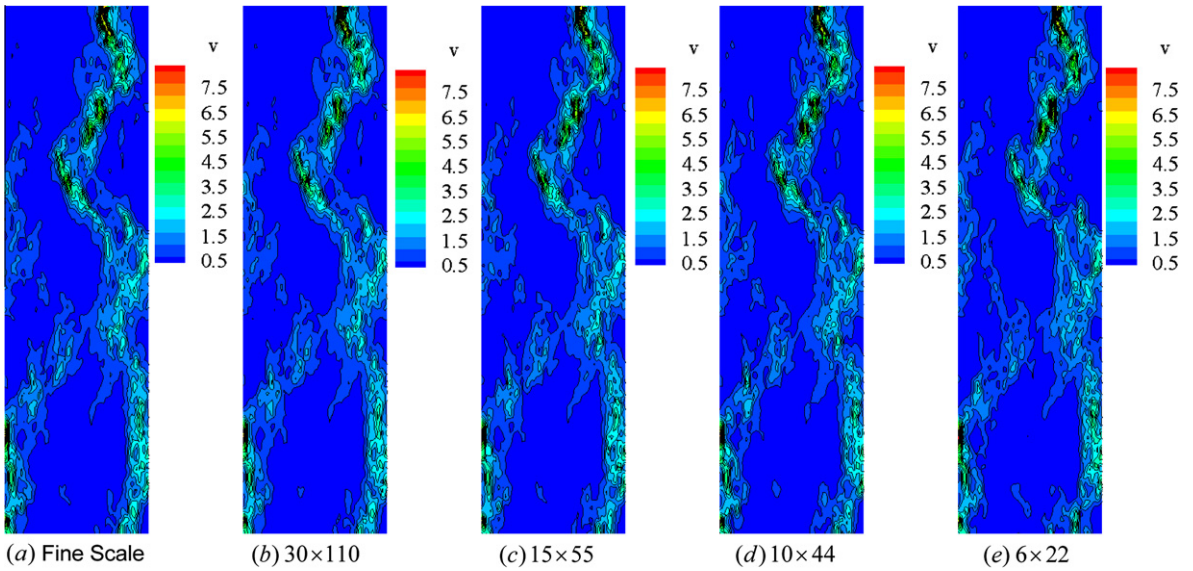

Fig. 7. Contour plots of the *y*-velocity component for various meshes: (a) 60×220 fine-scale grid, (b) 30×110 coarse grid, (c) 15×55 coarse grid, (d) 10×44 coarse grid, and (e) 6×22 coarse grid.

Table 1
Relative errors for various coarse grids in Example 1.

Errors	30×110	15×55	10×44	6×22
$\delta(\boldsymbol{u})$	0.112	0.159	0.170	0.234
$\delta(S)$	0.025	0.049	0.067	0.124
$\delta(F)$	0.0033	0.0019	0.0101	0.0165

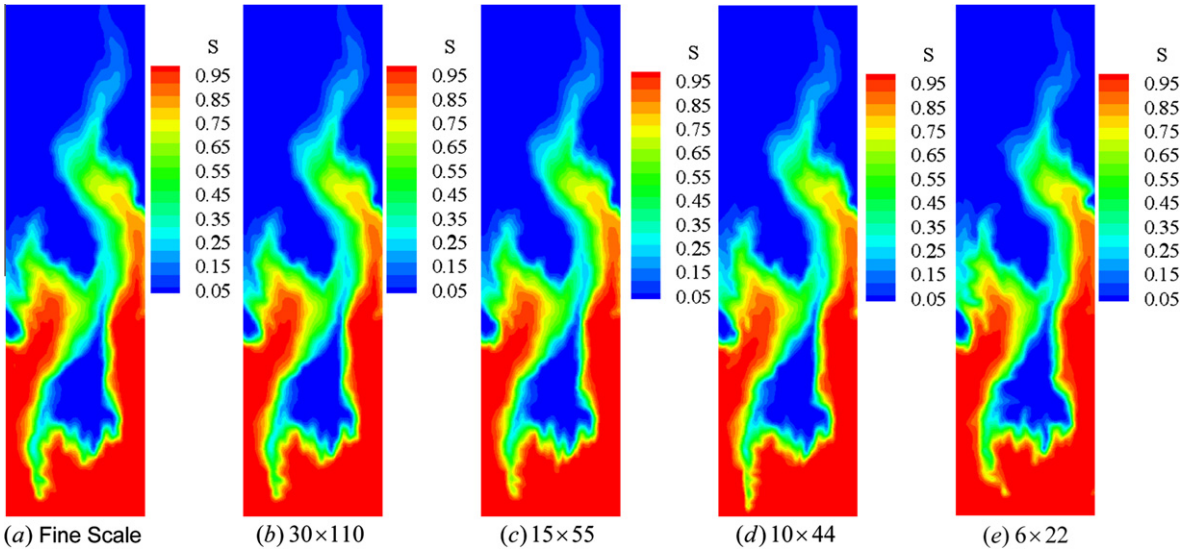

Fig. 8. Contour plots of saturation at 0.4 PVI: (a) 60×220 fine-scale grid, (b) 30×110 coarse grid, (c) 15×55 coarse grid, (d) 10×44 coarse grid, and (e) 6×22 coarse grid.

However, for reservoir simulation the most crucial factor is the transport properties of a velocity field. That is, a large local error in the velocity field may not be crucial as long as the overall transport properties are correct. Therefore, we give the contour plots of the saturation at time 0.4 PVI for various coarse grids in Fig. 8. The four multiscale results compare very well with the reference solution. To assess the accuracy of the transport properties, we measure the relative difference in the saturation profile at a given time: $\delta(S) = (\int_D |S_{\text{ref}} - S_{\text{ms}}|^2 d\boldsymbol{x})^{1/2} / (\int_D |S_{\text{ref}}|^2 d\boldsymbol{x})^{1/2}$. The result is given in Table 1. It is seen that although the corresponding velocity error is larger for the same coarse grid, the saturation error is significantly smaller.

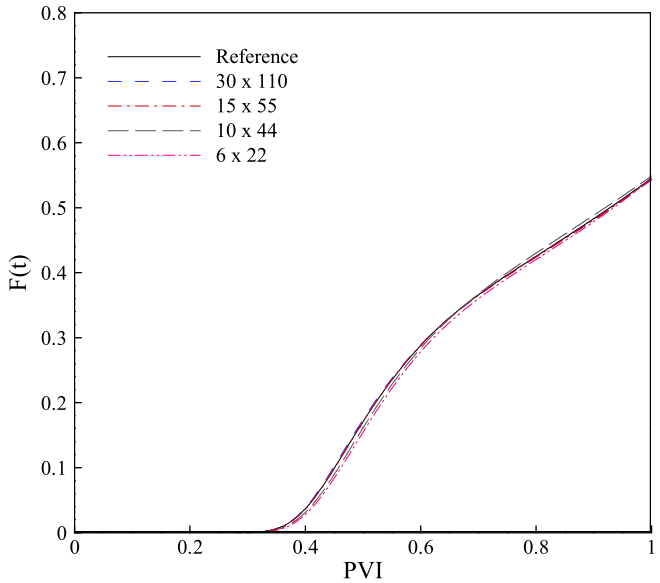

Fig. 9. Water cut curves for various coarse grids.

Table 2
Computational time (in seconds) for fine and various coarse grids in Example 1. The fine scale solver (single-scale mixed FEM solver) is the column corresponding to a grid of 60×220.

# Processor	60×220	30×110	15×55	10×44	6×22
1	50	120	73	60	55
2	44	76	44	38	33
4	42	53	33	30	26

Next, we consider the water cut, which is shown in Fig. 9. Once again, the results compare well with the reference solution. Here, we measure the maximum error as $\delta(F) = \max_{t \geqslant 0} |F_{\text{ref}}(t) - F_{\text{ms}}(t)|$. The result is shown in Table 1, where the error is quite small. Note that this is a quite strict measure, since the water cut curves tend to be steep right after breakthrough, and thus a small deviation in breakthrough time may give a large value in the error measure.

Finally, we want to comment on the computational cost of the multiscale method. The result is shown in Table 2. If only one processor is used, the computational cost of the MxHMM is comparable to that of the fine scale solver. In particular, when the coarse-scale mesh has nearly the same resolution as the fine mesh, the computational cost is even higher. However, as discussed in [18], the target of multiscale methods is not aimed at solving only one single elliptic equation such as the current single-phase flow problem, but at multiphase flow simulations where multiple solutions of elliptic problems are needed. In this case, we do not need to solve the fine-scale problem at each time step. Instead, we only need to reconstruct the fine-scale velocity using the initial coarse-scale solution with adaptive simulation algorithm [10,11,13,14,18]. This is an important problem and we would like to discuss the extension of our method to multi-phase flows in a separate work while keeping the current presentation focus on stochastic simulation. It should also be noted that our method is almost trivial to parallelize. The results when using multiple processors are also shown in Table 2. It is seen that the computation time of the fine scale solver does not change significantly when increasing the number of processors. On the other hand, the computation time for the MxHMM reduces. This reduction is noticeable for very coarse grids, e.g. nearly 50% reduction on four processors for the grid $[6 \times 22]$ versus the grid $[60 \times 220]$. This is possible because we can solve each subgrid problem in parallel and the size of the global linear system of equations is also small. It should be noted that although the overall computation time of MxHMM method using 4 processors on coarse grid $[6 \times 22]$ is less than that of solving the fine-scale model directly, the computational speedup remains moderate.

Overall, through this example, it is shown that the introduced multiscale method is quite robust and accurate for different mesh discretizations.

5.2. Simulation in a realization sample from a random permeability field

In this section, we consider only a sample realization from a random permeability field, which can be considered as a deterministic run at a collocation point in a stochastic simulation. The permeability is defined on a 100×100 fine-scale grid, which is shown in Fig. 10. Flow is induced from left-to-right with Dirichlet boundary conditions $\bar{p} = 100$ on $\{x_1 = 0\}$, $\bar{p} = 0$ on

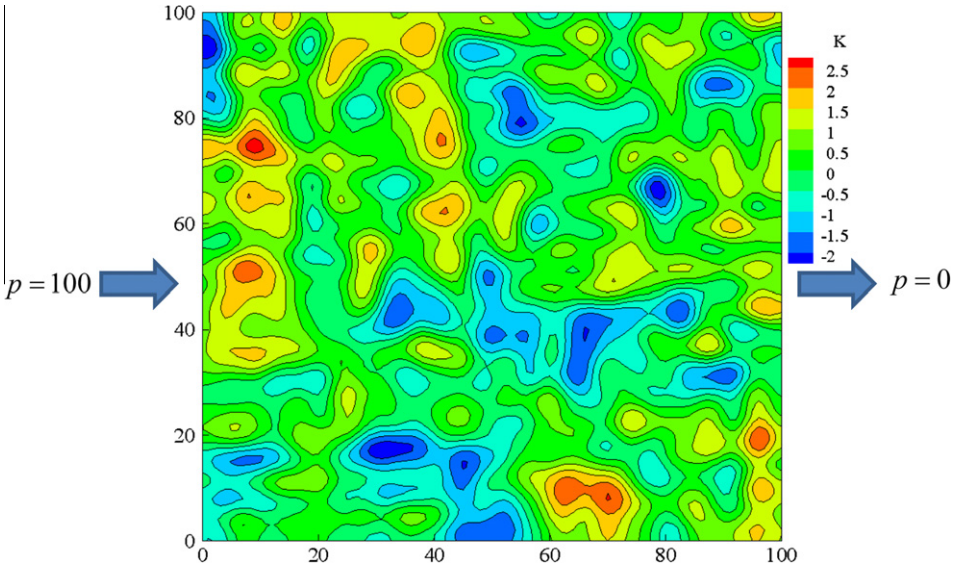

Fig. 10. Logarithm of the permeability field from one sample of a log-normal permeability filed defined on 100×100 fine-scale grid.

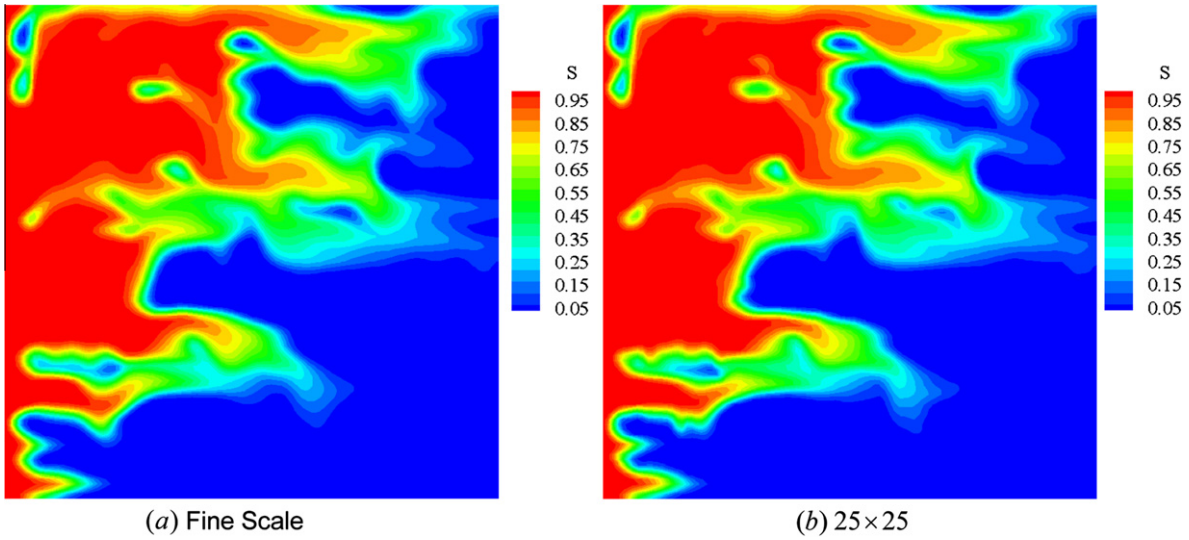

Fig. 11. Contour plots of saturation at 0.4 PVI: for (a) 100×100 fine-scale grid and (b) 25×25 coarse grid.

Table 3
Relative errors for various coarse grids in Example 2.

Errors	50×50	25×25	20×20	10×10
$\delta(\boldsymbol{u})$	0.060	0.156	0.183	0.324
$\delta(S)$	0.019	0.065	0.089	0.182
$\delta(F)$	0.0017	0.0059	0.0149	0.0079

$\{x_1 = 100\}$ and no-flow homogeneous Neumann boundary conditions on the other two edges. We also impose zero initial condition for saturation $S(x,0) = 0$ and boundary condition $S(x,t) = 1$ on the inflow boundary $\{x_1 = 0\}$. The reference solution is again taken from the single-scale mixed finite element on the fine-scale grid directly. All the errors are defined the same as before.

The saturation plot at time 0.4 PVI is shown in Fig. 11 which compares well with the reference solution. The relative errors are shown in Table 3. We note the relatively small saturation errors compared with the large velocity errors, which

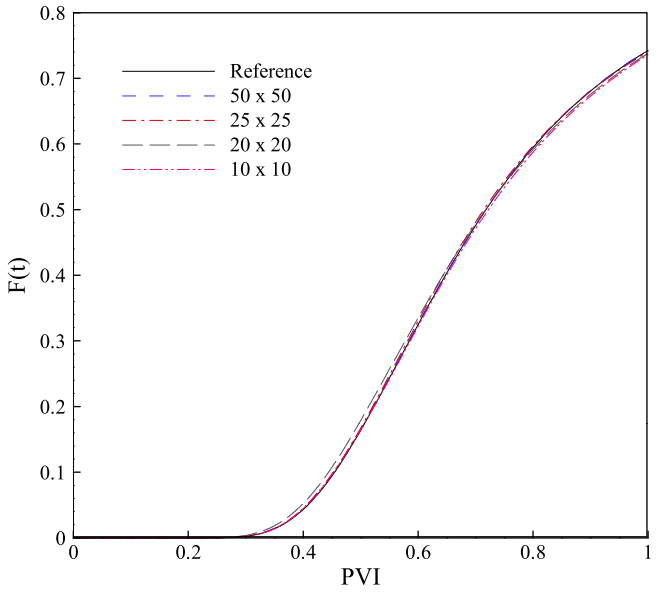

Fig. 12. Water cut curves for various coarse grids.

again confirms that the large local velocity errors may not reflect the overall accuracy of the saturation results as long as the multiscale method captures the major feature of the underlying permeability field.

Water cut curves are shown in Fig. 12 and the maximum error is given in Table 3. All the water cut curves are visually nearly the same. The two deterministic numerical examples successfully validate the introduced multiscale model. Since the stochastic multiscale framework only requires repeated solution of the deterministic problems at different collocation points, it is expected to also have accurate statistics of the solution in the stochastic simulation as shown in the next example.

5.3. Simulation in random permeability field

In the last two examples, we have successfully verified the accuracy of our newly developed multiscale solver. In this example, we investigate the statistical properties of the transport phenomena in random heterogeneous porous media. The domain of interest is the unit square $[0,1]^2$. Flow is still induced from left-to-right with Dirichlet boundary conditions $\bar{p} = 1$ on $\{x_1 = 0\}, \bar{p} = 0$ on $\{x_1 = 1\}$ and no-flow homogeneous Neumann boundary conditions on the other two edges. We also impose zero initial condition for saturation $S(x,0) = 0$ and boundary condition $S(x,t) = 1$ on the inflow boundary $\{x_1 = 0\}$.

The log-permeability is taken as zero mean random field with a separable exponential covariance function

$$\mathrm{Cov}(\boldsymbol{x},\boldsymbol{y}) = \sigma^2 \exp\left(-\frac{|x_1 - y_1|}{L_1} - \frac{|x_2 - y_2|}{L_2}\right), \tag{63}$$

where L_1 and L_2 are the correlation lengths in x and y direction, respectively. σ is the standard deviation of the random field. The K–L expansion is used to parameterize the field as

$$\mathbf{Y}(\omega) = \log(K(\omega)) = \sum_{i=1}^{N} \sqrt{\lambda_i}\phi_i(\boldsymbol{x})Y_i, \tag{64}$$

where the eigenvalues λ_i, $i = 1,2,\ldots$, and their corresponding eigenfunctions ϕ_i, $i = 1,2,\ldots$, can be determined analytically as discussed in [37]. Different probability distributions can be chosen for Y_i. The effects of log permeability with uniform, beta and Gaussian distributions on the mean and standard deviation of the output were investigated in [38], where the results showed that the three distributions had close peak values of standard deviation. Therefore, without losing the main feature of the output uncertainty, here Y_i are assumed as i.i.d. uniform random variables on $[-1, 1]$.

In this problem, the fine-scale permeability is defined on 64×64 grid and the coarse grid is taken as 8×8. For comparison, the reference solution is taken from 10^6 MC samples, where each direct problem is solved using the fine-scale solver. The stochastic problem is solved using HDMR, where the solution of each deterministic problem at the collocation points is from the multiscale solver. In this way, the accuracy of both multiscale solver and HDMR can be verified. In our previous work [44], the effects of the correlation length and standard deviation have been studied thoroughly. Thus, here we will fix the standard deviation to $\sigma^2 = 1.0$ and investigate the effect of the anisotropy of the random field.

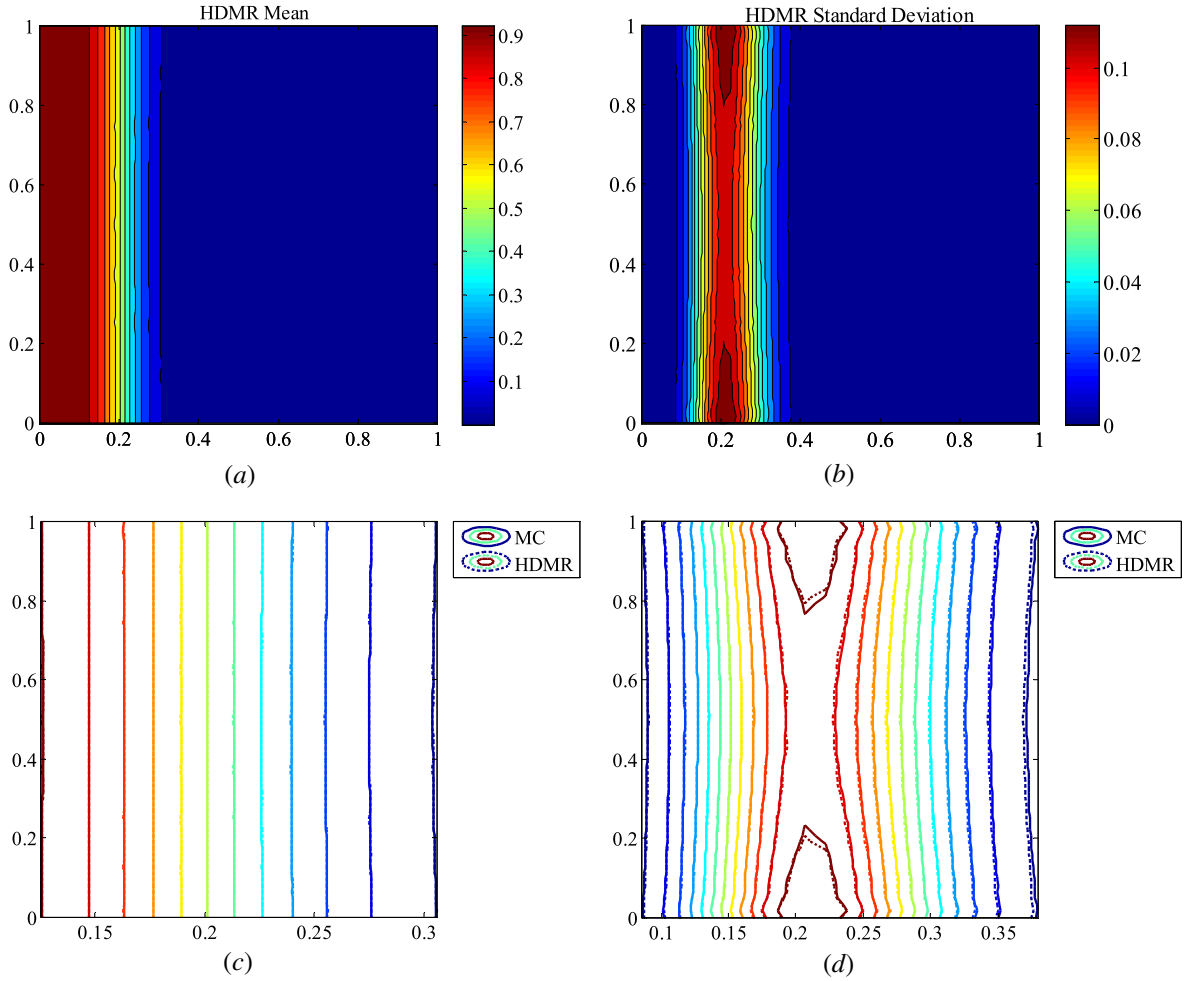

Fig. 13. Mean and standard deviation of saturation at 0.2 PVI for isotropic random field. Top: mean (a) and standard deviation (b) form HDMR. Bottom: comparison of mean (c) and standard deviation (d) between MC and HDMR near the saturation front.

5.3.1. Isotropic random field

In this problem, we take $L_1 = L_2 = 0.1$. Due to the slow decay of the eigenvalues, Eq. (64) is truncated after 100 terms. Therefore, the stochastic dimension is 100. The problem is solved with HDMR where each sub-problem is solved through ASGC. We take $\varepsilon = 10^{-6}$, $\theta_1 = 5 \times 10^{-5}$ and $\theta_2 = 10^{-4}$.

In Fig. 13, we compare the mean and standard deviation at 0.2 PVI. It is interesting to note that although the permeability field shows heterogeneity for different realizations, the mean saturation is the same as the solution with homogeneous mean permeability field. This behavior is called "heterogeneity-induced dispersion" where the heterogeneity smoothes the water saturation profile in the ensemble sense. Our results again confirms this phenomenon, which was first investigated in [32] through method of moment equations. The figure also indicates that higher water saturation variations are concentrated near displacement fronts, which are areas of steep saturation gradients. Therefore, the comparisons between the MC and HDMR results are only shown around the displacement fronts on the bottom two plots in Fig. 13. It is seen that the solutions from HDMR compare quite well with the Monte Carlo results. The convergence of HDMR is shown in Table 4, where the normalized error is defined the same as before with MC results as the reference solution. N_i denotes the number of important dimensions and N_c denotes the total number of component functions. The expansion order of HDMR for all three cases is 2. For conventional HDMR, the total number of component functions is 5051. However, by using adaptivity, N_c is reduced to 1047 which clearly demonstrates the advantage of our methods. From the table, it is seen that the results are indeed quit accurate despite the fact that 64-fold upscaling is used to solve the deterministic problem and adaptive methods are used to solve the stochastic problem.

Next, we demonstrate the interpolatory properties of the HDMR method. As mentioned before, one of the advantages of HDMR is that it can serve as a surrogate model for the original problem. Realization of the saturation for arbitrary random input can be obtained through HDMR. To verify this property, we randomly generate one input vector and reconstruct the result from HDMR. At the same time, we run a deterministic problem with the fine-scale model and the same realization of

Table 4
Convergence of HDMR with different θ_1 at 0.2 PVI for isotropic random field.

θ_1	N_i	N_c	# Points	Error mean	Error std.
1×10^{-3}	2	102	1694	7.47×10^{-4}	4.38×10^{-2}
1×10^{-4}	27	452	34379	5.69×10^{-4}	2.06×10^{-2}
5×10^{-5}	44	1047	77988	5.10×10^{-4}	6.66×10^{-3}

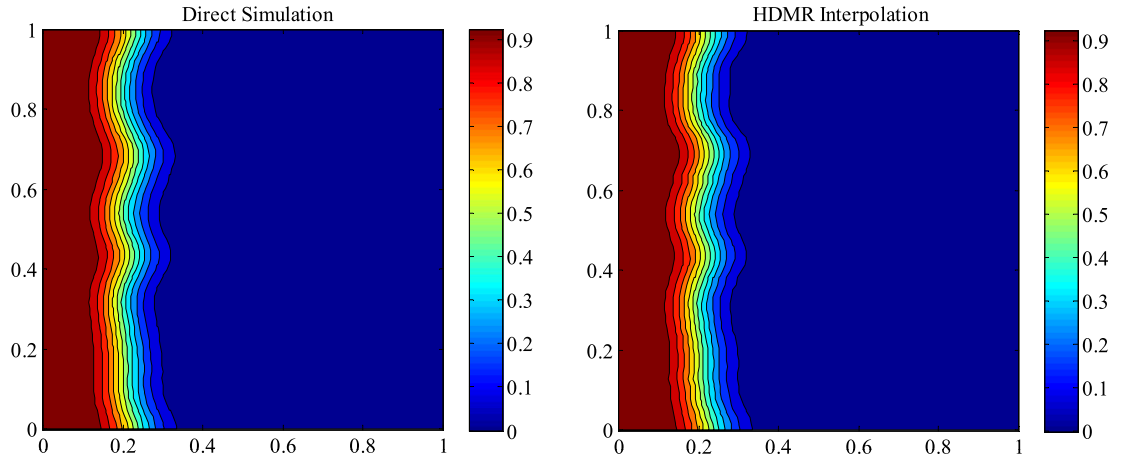

Fig. 14. Prediction of the saturation profile using HDMR and the solution of the deterministic fine-scale problem with the same input for isotropic random field. Left: saturation at 0.2 PVI from direct simulation, Right: saturation at 0.2 PVI reconstructed from HDMR.

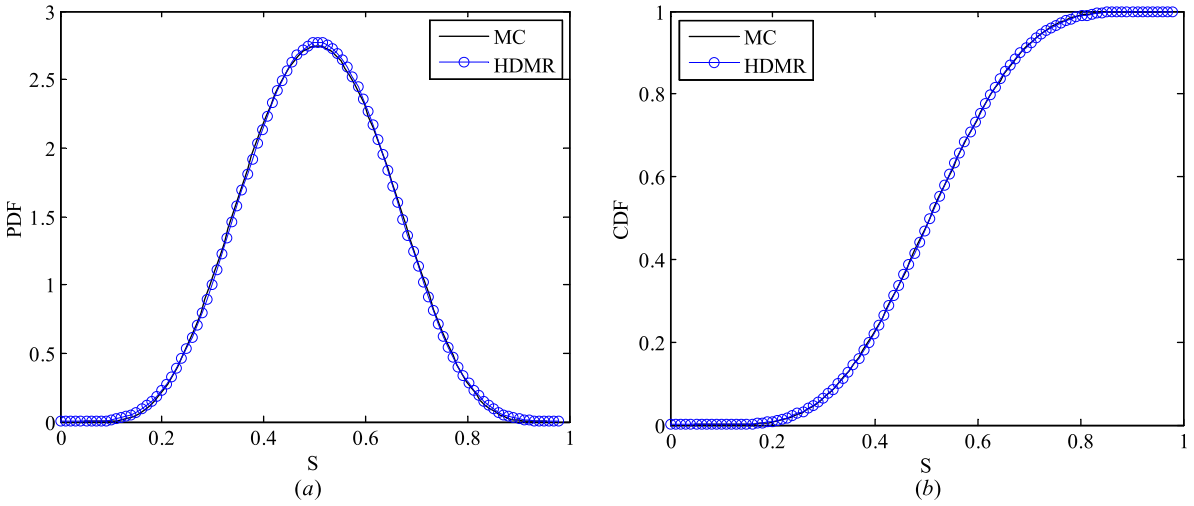

Fig. 15. Isotropic random field: (a) PDF of the saturation at point (0.2, 0) and 0.2 PVI, (b) CDF of the saturation at point (0.2,0) and 0.2 PVI.

the random input vector. The comparison of these results are shown in Fig. 14. In addition, in Fig. 15, we also plot the probability density function (PDF) and cumulative distribution function (CDF) at point (0.2, 0) where it has the highest standard deviation as indicated from Fig. 13(b). These results indicate that the corresponding HDMR approximations are indeed very accurate. Therefore, we can obtain any statistics from this stochastic reduced-order model, which is an advantage of the current method over the MC method.

Similar results at 0.4 PVI are also given in Figs. 16–18, respectively. It is noted that the standard deviation of the saturation becomes larger at later time as is seen from the wider strip of the non-zero regions in the contour maps at 0.4 PVI in Fig. 16. With the increase of the standard deviation, more collocation points are needed to capture the overall uncertainty. Indeed, there are 1229 component functions and 104,662 collocation points in this case. From Fig. 17, it is seen that the saturation front exhibits a much more significant variation due to the larger standard deviation. Similarly, in Fig. 18, we plot the PDF

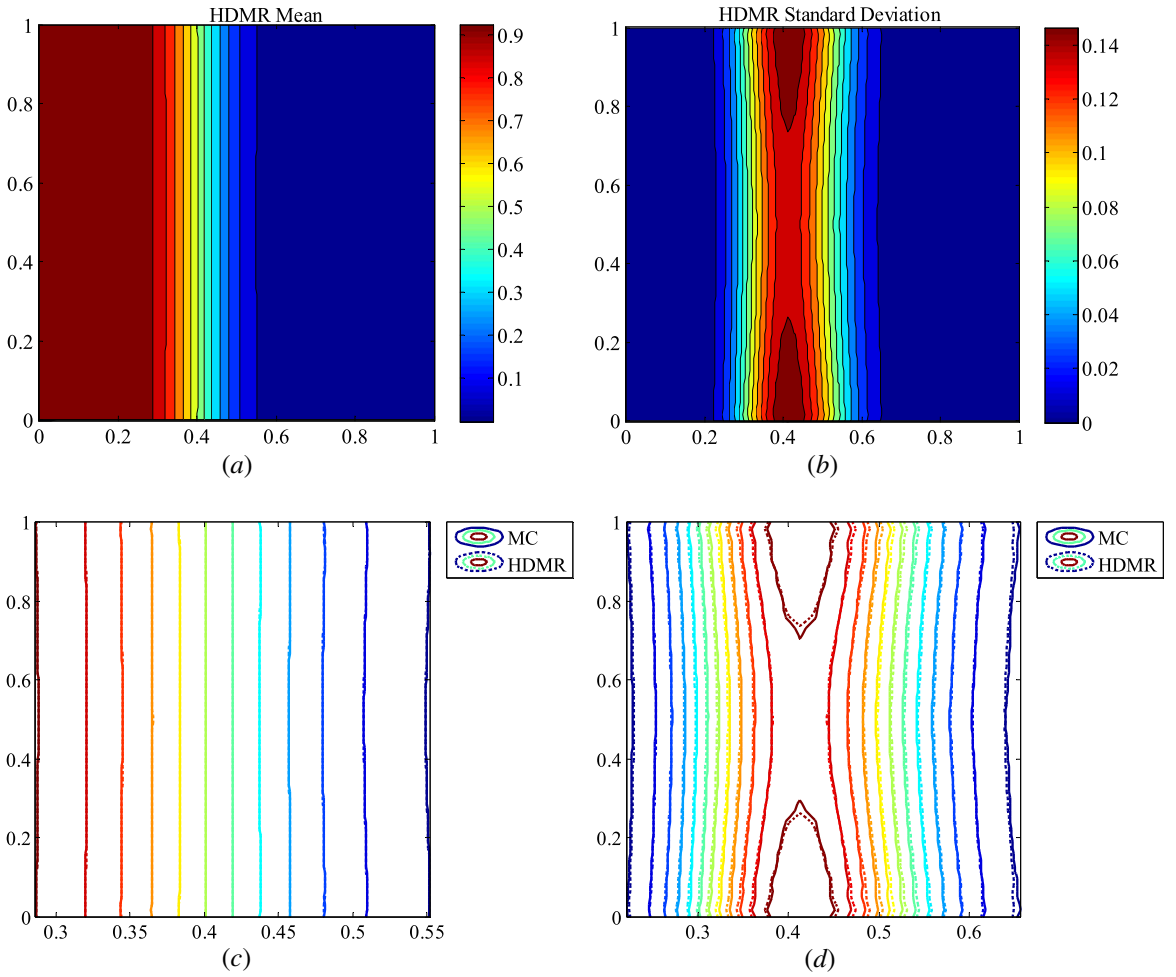

Fig. 16. Mean and standard deviation of saturation at 0.4 PVI for isotropic random field. Top: mean (a) and standard deviation (b) form HDMR. Bottom: comparison of mean (c) and standard deviation (d) between MC and HDMR near the saturation front.

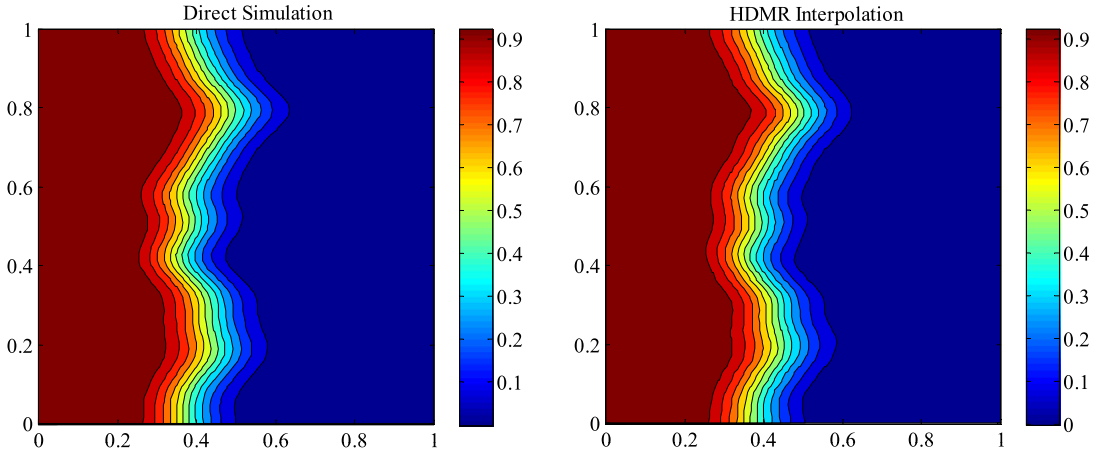

Fig. 17. Prediction of the saturation profile using HDMR and the solution of the deterministic fine-scale problem with the same input for isotropic random field. Left: saturation at 0.4 PVI from direct simulation, Right: saturation at 0.4 PVI reconstructed from HDMR.

and CDF at point (0.4,0) where the highest standard deviation happens. It is noted that the spread of the PDF at 0.4 PVI is wider than that of 0.2 PVI which again indicates the larger variation of the saturation at this time step. Thus, it is more difficult to predict the uncertainty with the simulation time increases.

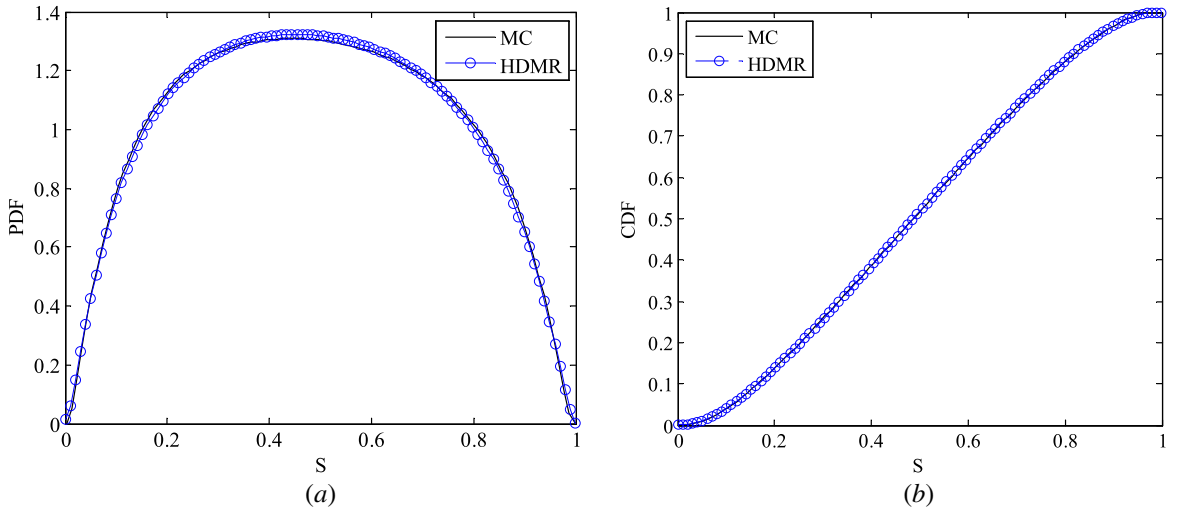

Fig. 18. Isotropic random field: (a) PDF of the saturation at point (0.4, 0) and 0.4 PVI and (b) CDF of the saturation at point (0.4, 0) and 0.4 PVI.

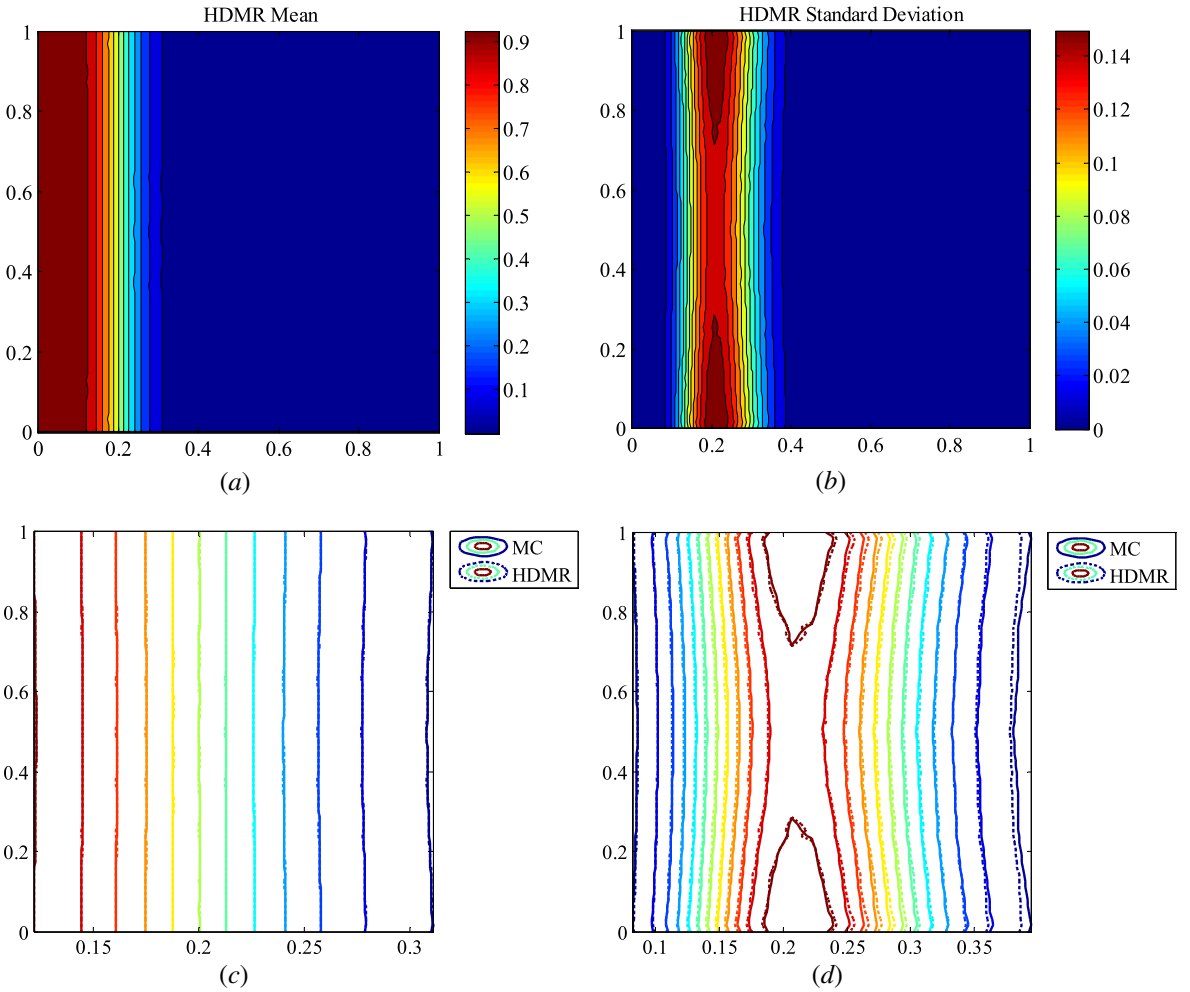

Fig. 19. Mean and standard deviation of saturation at 0.2 PVI for anisotropic random field. Top: mean (a) and standard deviation (b) form HDMR. Bottom: comparison of mean (c) and standard deviation (d) between MC and HDMR near the saturation front.

Table 5
Convergence of HDMR with different θ_1 at 0.2 PVI for anisotropic random field.

θ_1	N_i	N_c	# Points	Error mean	Error std.
1×10^{-3}	8	79	6199	1.14×10^{-3}	4.69×10^{-2}
1×10^{-4}	38	754	72243	6.95×10^{-4}	1.35×10^{-2}
5×10^{-5}	45	1044	96999	6.51×10^{-4}	1.01×10^{-2}

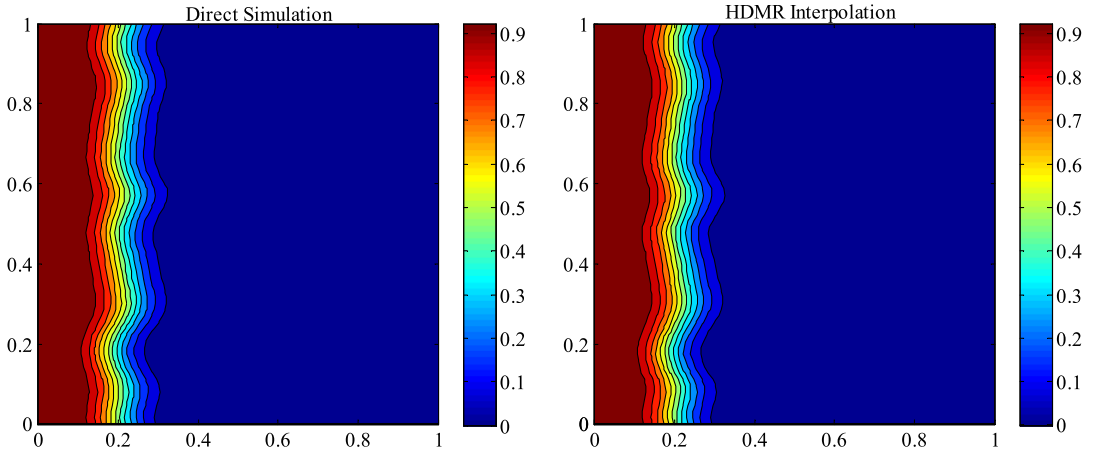

Fig. 20. Prediction of the saturation profile using HDMR and the solution of the deterministic fine-scale problem with the same input for anisotropic random field. Left: saturation at 0.2 PVI from direct simulation, Right: saturation at 0.2 PVI reconstructed from HDMR.

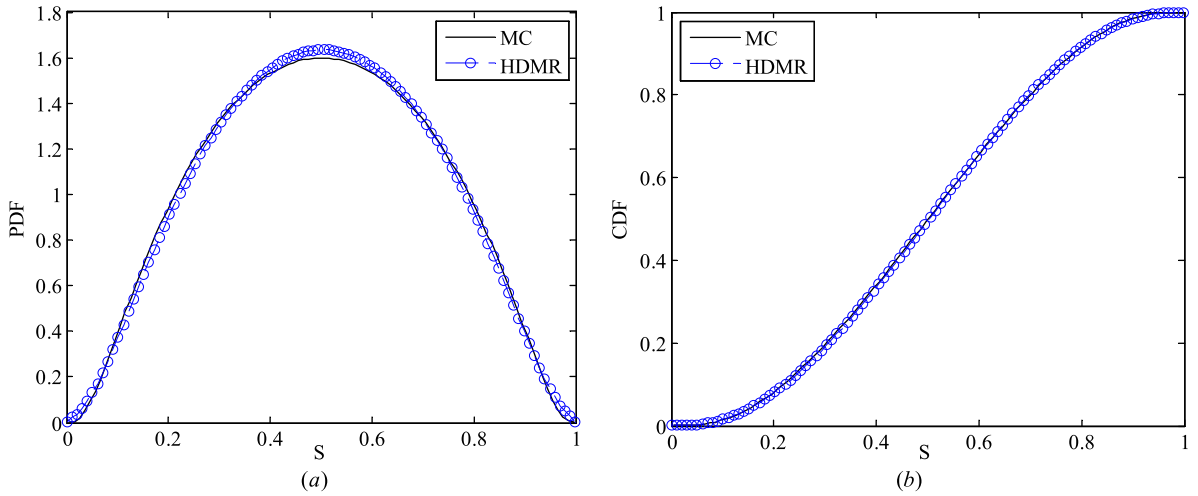

Fig. 21. Anisotropic random field: (a) PDF of the saturation at point (0.2,0) and 0.2 PVI, (b) CDF of the saturation at point (0.2,0) and 0.2 PVI.

5.3.2. Anisotropic random field

In this problem, we take $L_1 = 0.25$, $L_2 = 0.1$. Due to the increase of the correlation length in the x direction, Eq. (64) is truncated after 50 terms. Therefore, the stochastic dimension is taken as 50.

We first solve this problem at time 0.2 PVI using HDMR with ASGC. We take $\varepsilon = 10^{-6}$, $\theta_1 = 5 \times 10^{-5}$ and $\theta_2 = 10^{-4}$. The results are shown in Fig. 19. It is interesting to note that the shape of contours is nearly the same as that of the isotropic random field. Only the values of standard deviation are different. The introduction of anisotropy has the effect of increasing the output uncertainty. The convergence of HDMR is shown in Table 5. Again, the HDMR results compare very well with the reference solution. According to our previous numerical results in [44], larger uncertainty requires more expansion terms. Indeed, more expansion terms and collocation points are needed compared with that of the isotropic case. In addition, the highest HDMR expansion order is 3. There are 3 third-order component functions, which indicates the existence of

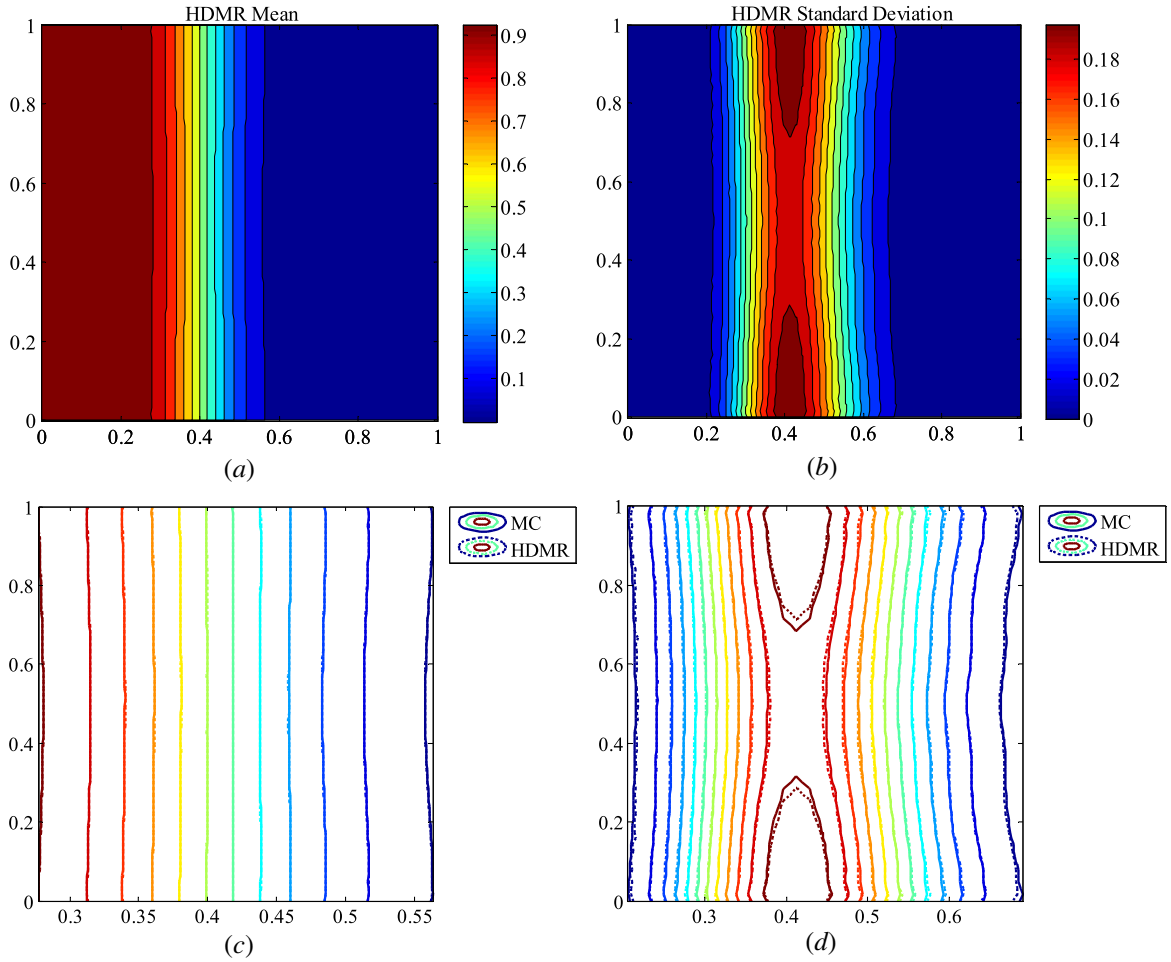

Fig. 22. Mean and standard deviation of saturation at 0.4 PVI for anisotropic random field. Top: mean (a) and standard deviation (b) form HDMR. Bottom: comparison of mean (c) and standard deviation (d) between MC and HDMR near the saturation front. Here each sub-problem is solved using sparse grid based on Gauss–Legendre quadrature rule.

Table 6
Convergence of HDMR with different θ_1 at 0.4 PVI for anisotropic random field.

θ_1	N_i	N_c	Order	# Points	Error mean	Error std.
1×10^{-3}	10	96	2	4126	1.32×10^{-3}	5.17×10^{-2}
1×10^{-4}	38	763	3	54925	7.00×10^{-4}	4.10×10^{-2}
5×10^{-5}	45	1087	3	82407	6.40×10^{-4}	3.21×10^{-2}
1×10^{-5}	50	2050	4	218136	2.97×10^{-4}	1.97×10^{-2}

higher-order cooperative effects among the inputs. The reconstruction of the saturation profile is shown in Fig. 20. The PDF and CDF at point (0.2,0) are shown in Fig. 21.

Finally, we show that HDMR is indeed a versatile method where each sub-problem can be solved by any stochastic method. Therefore, we solve the problem at 0.4 PVI using HDMR where each sub-problem is solved with sparse grid based on Gauss–Legendre quadrature rule instead of ASGC. A level three sparse grid is chosen for each sub-problem. θ_1 is chosen as 1×10^{-5}. The results are shown in Fig. 22. The convergence of HDMR is given in Table 6. In this extreme case, all the 50 dimensions are considered as important and the maximum expansion order is 4. This again is consistent with our previous results in [44]. Higher-order terms are needed to capture the large variability. Without adaptivity, there are 251,176 component functions for a 4th order conventional HDMR. The advantage of adaptive HDMR is more impressive in this case. We also solve this problem directly with a 50-dimensional sparse grid based on Gauss–Legendre quadrature rule. The results from levels 2 and 3 sparse grids are given in Fig. 23. Since the mean saturations are nearly the same, we only show the comparison between standard deviations. For level 2 sparse grid, the number of collocation points is 5301

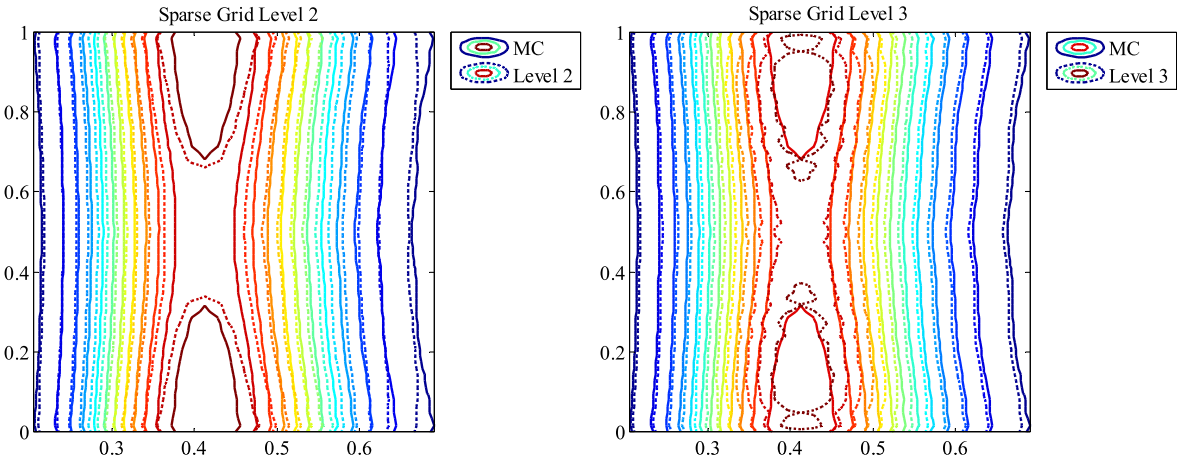

Fig. 23. Standard deviation of saturation at 0.4 PVI for anisotropic random field using 50-dimensional sparse grid based on Gauss–Legendre rule: comparison of standard deviation between MC and sparse grid level 2 (left) and 3 (right) near the saturation front.

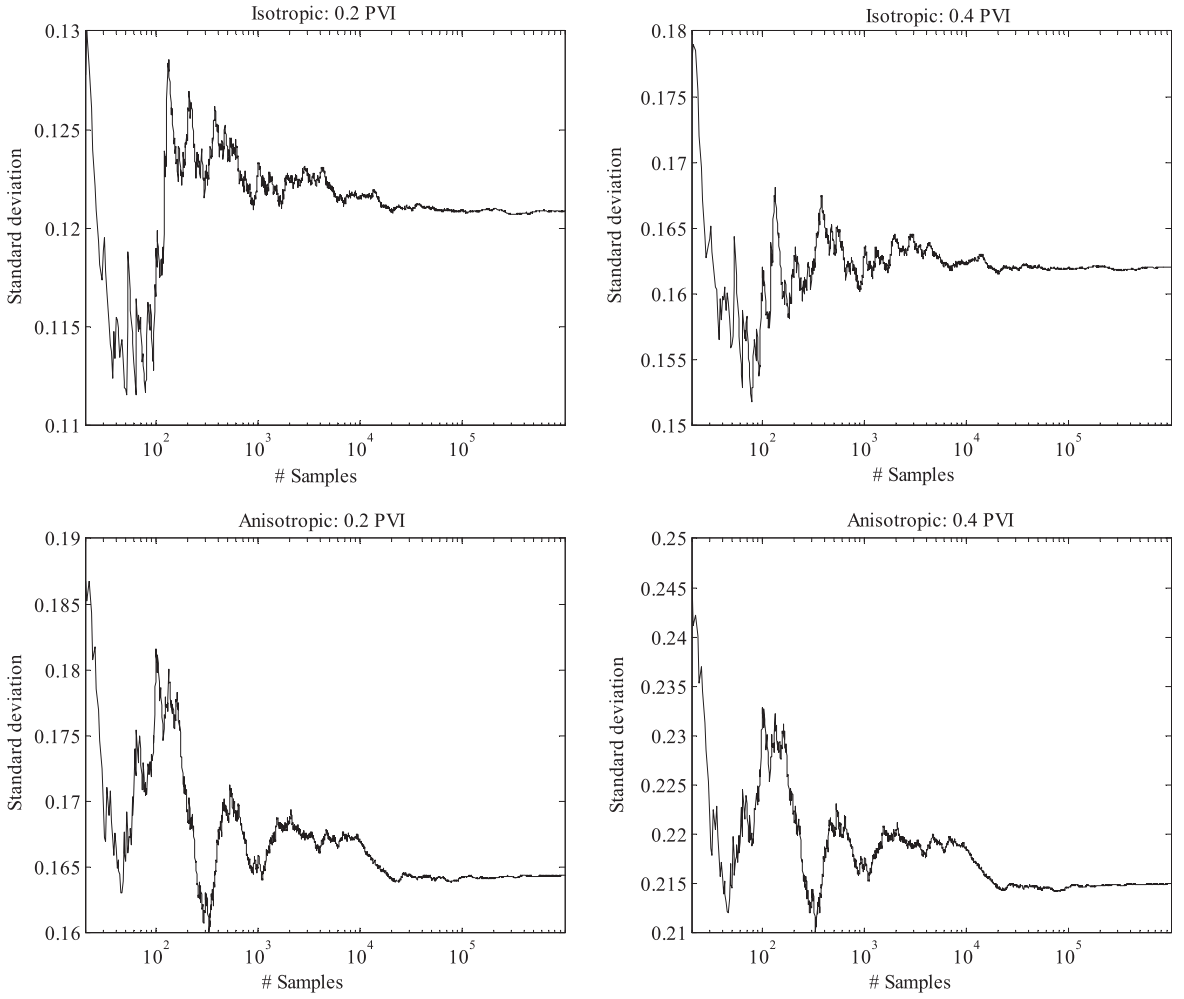

Fig. 24. Standard deviation of the saturation at the point, where the largest value occurs, obtained from MC simulations versus the number of realizations.

with the mean error 8.31×10^{-4} and std error 4.38×10^{-2}. However, when increasing the sparse grid to level 3 with a total number of 192201 collocation points, the mean error increases to 1.90×10^{-3} and std error increases to 7.09×10^{-2}. In other words, the direct sparse grid method fails to converge. It is computationally prohibiting to increase the sparse grid level to 4

since it would require 5,402,401 collocation points. The failure of convergence is due to the steep saturation gradient near the displacement front. For such problems, it is widely known that the polynomial based quadrature method has difficulty in convergence. From the results shown, it seems that the adaptive HDMR can reduce the irregularity of the stochastic space through decomposition of the dimensions. However, a higher order expansion may be needed at a significant increase in the computational cost.

Finally, we want to comment on the computational time of this example. First, in Fig. 24, the convergence of standard deviation of the saturation at one point with the number of MC simulations is given. The points are chosen at the place where the largest standard deviation occurs and they are different for different cases. From the figure, it is seen that at least 10^5 MC samples are needed in order to achieve statistical convergence. However, there are still some small oscillations after it. As is well known, the MC convergence rate is $M^{-1/2}$, therefore, to ensure a good comparison with HDMR, we use 10^6 samples eventually. It took about 19 h on 60 processors while the average computational time for HDMR is 5 h on the same number of processors in such a high-dimensional case. It is also noted from the figure that much more points are needed to achieve statistical convergence in the anisotropic case which partially explains the larger variations of saturation as was seen earlier. Moreover, an interesting observation is that the shapes of the convergence plots are nearly the same at the two time instants for the same random input. This phenomenon suggests that although the convergence rate of MC is independent of the number of stochastic dimensions, it does depend on the regularity of the stochastic input space. In general, more MC samples are needed for a stochastic space which is not smooth as is seen from the case of the anisotropic random field.

6. Conclusions

In the first part of this paper, a new multiscale methodology using the mixed finite element method is developed for the solution of elliptic equation arising from the heterogeneous porous media flow problem. This multiscale methodology is based on the framework of the heterogeneous multiscale method. A novel boundary condition for the local cell problem is proposed which gives more realistic flow conditions across a coarse-element interface. In addition, a reconstruction method for the fine-scale velocity is also proposed, which ensures the continuity of the mass at both local and global scales. The first two numerical examples considered verify the accuracy of the new method. However, as a first step towards this new method, only a single-phase flow and transport problem are considered. Our ongoing research includes investigating the multi-phase flow and incorporating the multiscale source terms and well modeling.

In the second part of this paper, we considered uncertainty quantification when the permeability field is modeled as a random field. The newly developed multiscale method is used as a direct solver within the framework of ASGC and HDMR. Our numerical results in Example 3 compare well with the MC results with fine-scale solvers, which again verifies the accuracy of both multiscale and HDMR methods. Our study confirms the interesting phenomenon that the introduction of permeability heterogeneity leads to the heterogeneity-induced dispersion. The obtained results also indicate that the HDMR expansion can serve as an accurate surrogate model for the underlying stochastic problem.

The input uncertainty in the permeability considered in the current work is defined from an analytical KL expansion with known covariance which only represents two-point statistics. In our recent work, we are considering data-driven stochastic input models which can generate more realistic permeability fields with higher-order statistics. This work is reported in a separate paper [63]. The model from [63] can be used as an alternate input into the developed stochastic multiscale framework. Research quantifying the uncertainty in such cases is in progress.

Acknowledgements

This research was supported by the US Department of Energy, Office of Science, Advanced Scientific Computing Research, the Computational Mathematics program of the National Science Foundation (NSF) (award DMS-0809062) and an OSD/AFOSR MURI09 award on uncertainty quantification. The computing for this research was supported by the NSF through TeraGrid resources provided by NCSA under Grant No. TG-DMS090007.

References

[1] T.Y. Hou, X.-H. Wu, A multiscale finite element method for elliptic problems in composite materials and porous media, Journal of Computational Physics 134 (1) (1997) 169–189.
[2] T.Y. Hou, X.-H. Wu, Z. Cai, Convergence of a multiscale finite element method for elliptic problems with rapidly oscillating coefficients, Mathematics of Computation 68 (1999) 913–943.
[3] Y. Efendiev, T.Y. Hou, Multiscale Finite Element: Theory and Applications, Springer, New York, 2009.
[4] T.J.R. Hughes, Multiscale phenomena: Green's functions, the Dirichlet-to-Neumann formulation, subgrid scale models, bubbles and the origins of stabilized methods, Computer Methods in Applied Mechanics and Engineering 127 (1995) 387–401.
[5] T.J.R. Hughes, G.R. Feijo, L. Mazzei, J.-B. Quincy, The variational multiscale method – a paradigm for computational mechanics, Computer Methods in Applied Mechanics and Engineering 166 (1998) 3–24.
[6] E. Weinan, B. Engquist, The heterogeneous multi-scale methods, Communications in Mathematical Physics 1 (2002) 87–132.
[7] E. Weinan, B. Engquist, X. Li, W. Ren, E. Vanden-Eijnden, Heterogeneous multiscale methods: a review, Communications in Computational Physics 2 (2007) 367–450.
[8] Z. Chen, T.Y. Hou, A mixed multiscale finite element method for elliptic problems with oscillating coefficients, Mathematics of Computation 72 (2003) 541–576.

[9] P. Raviart, J. Thomas, A mixed finite element method for 2-nd order elliptic problems, in: Galligani, E. Magenes (Eds.), Mathematical Aspects of Finite Element Methods, Lecture Notes in Mathematics, vol. 606, Springer-Verlag, 1977, pp. 292–315.
[10] J.E. Aarnes, On the use of a mixed multiscale finite element method for greater flexibility and increased speed or improved accuracy in reservoir simulation, Multiscale Modeling and Simulation 2 (2004) 421–439.
[11] J.E. Aarnes, V. Kippe, K.-A. Lie, Mixed multiscale finite elements and streamline methods for reservoir simulation of large geomodels, Advances in Water Resources 28 (2005) 257–271.
[12] P. Jenny, S.H. Lee, H.A. Tchelepi, Multi-scale finite-volume method for elliptic problems in subsurface flow simulation, Journal of Computational Physics 187 (2003) 47–67.
[13] P. Jenny, S.H. Lee, H.A. Tchelepi, Adaptive multiscale finite-volume method for multiphase flow and transport in porous media, Multiscale Modeling and Simulation 3 (2005) 50–64.
[14] P. Jenny, S. Lee, H. Tchelepi, Adaptive fully implicit multi-scale finite-volume method for multi-phase flow and transport in heterogeneous porous media, Journal of Computational Physics 217 (2006) 627–641.
[15] T. Arbogast, Implementation of a locally conservative numerical subgrid upscaling scheme for two-phase Darcy flow, Computational Geosciences 6 (2002) 453–481.
[16] T. Arbogast, Analysis of a two-scale, locally conservative subgrid upscaling for elliptic problems, SIAM Journal on Numerical Analysis 42 (2004) 576–598.
[17] R. Juanes, F.-X. Dub, A locally conservative variational multiscale method for the simulation of porous media flow with multiscale source terms, Computational Geosciences 12 (2008) 273–295.
[18] V. Kippe, J.E. Aarnes, K.-A. Lie, A comparison of multiscale methods for elliptic problems in porous media flow, Computational Geosciences 12 (2008) 377–398.
[19] W. Ren, Heterogeneous multiscale method for the modeling of complex fluids and micro-fluidics, Journal of Computational Physics 204 (2005) 1–26.
[20] X. Li, Multiscale modeling of the dynamics of solids at finite temperature, Journal of the Mechanics and Physics of Solids 53 (2005) 1650–1685.
[21] A. Abdulle, C. Schwab, Heterogeneous multiscale FEM for diffusion problems on rough surfaces, Multiscale Modeling and Simulation 3 (2005) 195–220.
[22] A. Abdulle, A. Nonnenmacher, A short and versatile finite element multiscale code for homogenization problems, Computer Methods in Applied Mechanics and Engineering 198 (2009) 2839–2859.
[23] A. Abdulle, The finite element heterogeneous multiscale method: a computational strategy for multiscale PDEs, GAKUTO International Series Mathematical Sciences and Applications 31 (2009) 135–184.
[24] W. E, P. Ming, P. Zhang, Analysis of the heterogeneous multiscale method for elliptic homogenization problems, Journal of the American Mathematical Society 18 (2004) 121–156.
[25] A. Abdulle, On a priori error analysis of fully discrete heterogeneous multiscale FEM, Multiscale Modeling and Simulation 4 (2005) 447–459.
[26] A. Abdulle, A. Nonnenmacher, A posteriori error analysis of the heterogeneous multiscale method for homogenization problems, Comptes Rendus Mathematique 347 (2009) 1081–1086.
[27] Z. Chen, Multiscale methods for elliptic homogenization problems, Numerical Methods for Partial Differential Equations 22 (2006) 317–360.
[28] R. Ghanem, Probabilistic characterization of transport in heterogeneous media, Computer Methods in Applied Mechanics and Engineering 158 (1998) 199–220.
[29] R. Ghanem, Scales of fluctuation and the propagation of uncertainty in random porous media, Water Resources Research 34 (1998) 2123–2136.
[30] R. Ghanem, S. Dham, Stochastic finite element analysis for multiphase flow in heterogeneous porous media, Transport in Porous Media 32 (1998) 239–262.
[31] D. Zhang, Stochastic Method for Flow in Porous Media: Coping with Uncertainties, Academic Press, San Diego, 2002.
[32] D. Zhang, H. Tchelepi, Stochastic analysis of immiscible two-phase flow in heterogeneous media, SPE Journal 4 (1999) 380–388.
[33] D. Zhang, L. Li, H. Tchelepi, Stochastic formulation for uncertainty analysis of two-phase flow in heterogeneous reservoirs, SPE Journal 5 (2000) 60–70.
[34] K.D. Jarman, T.F. Russell, Eulerian moment equations for 2-d stochastic immiscible flow, Multiscale Modeling and Simulation 1 (2003) 598–608.
[35] B. Ganis, H. Klie, M.F. Wheeler, T. Wildey, I. Yotov, D. Zhang, Stochastic collocation and mixed finite elements for flow in porous media, Computer Methods in Applied Mechanics and Engineering 197 (2008) 3547–3559.
[36] H. Li, D. Zhang, Probabilistic collocation method for flow in porous media: comparisons with other stochastic methods, Water Resources Research 43 (2007) W09409.
[37] G. Lin, A. Tartakovsky, An efficient, high-order probabilistic collocation method on sparse grids for three-dimensional flow and solute transport in randomly heterogeneous porous media, Advances in Water Resources 32 (2009) 712–722.
[38] G. Lin, A. Tartakovsky, Numerical studies of three-dimensional stochastic Darcys equation and stochastic advection–diffusion–dispersion equation, Journal of Scientific Computing 43 (2010) 92–117.
[39] I. Babuška, F. Nobile, R. Tempone, A stochastic collocation method for elliptic partial differential equations with random input data, SIAM Journal on Numerical Analysis 45 (2007) 1005–1034.
[40] D. Xiu, J.S. Hesthaven, High-order collocation methods for differential equations with random inputs, SIAM Journal on Scientific Computing 27 (2005) 1118–1139.
[41] B. Ganapathysubramanian, N. Zabaras, Sparse grid collocation schemes for stochastic natural convection problems, Journal of Computational Physics 225 (2007) 652–685.
[42] F. Nobile, R. Tempone, C.G. Webster, A sparse grid stochastic collocation method for partial differential equations with random input data, SIAM Journal on Numerical Analysis 46 (2008) 2309–2345.
[43] X. Ma, N. Zabaras, An adaptive hierarchical sparse grid collocation algorithm for the solution of stochastic differential equations, Journal of Computational Physics 228 (2009) 3084–3113.
[44] X. Ma, N. Zabaras, An adaptive high-dimensional stochastic model representation technique for the solution of stochastic partial differential equations, Journal of Computational Physics 229 (2010) 3884–3915.
[45] G. Li, C. Rosenthal, H. Rabitz, High dimensional model representations, The Journal of Physical Chemistry A 105 (2001) 7765–7777.
[46] B.V. Asokan, N. Zabaras, A stochastic variational multiscale method for diffusion in heterogeneous random media, Journal of Computational Physics 218 (2006) 654–676.
[47] B. Ganapathysubramanian, N. Zabaras, Modeling diffusion in random heterogeneous media: data-driven models, stochastic collocation and the variational multiscale method, Journal of Computational Physics 226 (2007) 326–353.
[48] X.F. Xu, A multiscale stochastic finite element method on elliptic problems involving uncertainties, Computer Methods in Applied Mechanics and Engineering 196 (2007) 2723–2736.
[49] B. Ganapathysubramanian, N. Zabaras, A stochastic multiscale framework for modeling flow through random heterogeneous porous media, Journal of Computational Physics 228 (2009) 591–618.
[50] J.E. Aarnes, Y. Efendiev, Mixed multiscale finite element methods for stochastic porous media flows, SIAM Journal on Scientific Computing 30 (2008) 2319–2339.
[51] P. Dostert, Y. Efendiev, T. Hou, Multiscale finite element methods for stochastic porous media flow equations and application to uncertainty quantification, Computer Methods in Applied Mechanics and Engineering 197 (2008) 3445–3455.
[52] Z. Chen, Q. Du, An upwinding mixed finite element method for a mean field model of superconducting vortices, Mathematical Modelling and Numerical Analysis 34 (2000) 687–706.
[53] L.J. Durlofsky, Upscaling of geocellular models for reservoir flow simulation: a review of recent progress, in: 7 th International Forum on Reservoir Simulation, Baden-Baden, Germany, 2003.

[54] R. Ghanem, P.D. Spanos, Stochastic Finite Elements: A Spectral Approach, Springer-Verlag, New York, 1991.
[55] F. Brezzi, M. Fortin, Mixed and Hybrid Finite Element Method, Springer-Verlag, New York, 1991.
[56] X. Yue, W. E, The local microscale problem in the multiscale modeling of strongly heterogeneous media: effects of boundary conditions and cell size, Journal of Computational Physics 222 (2007) 556–572.
[57] X.H. Wen, L.J. Durlofsky, M.G. Edwards, Use of border regions for improved permeability upscaling, Mathematical Geology 35 (2003) 521–547.
[58] Y. Gautier, M. Blunt, M. Christie, Nested gridding and streamline-based simulation for fast reservoir performance prediction, Computational Geosciences 3 (1999) 295–320.
[59] S. Balay, K. Buschelman, W.D. Gropp, D. Kaushik, M.G. Knepley, L.C. McInnes, B.F. Smith, H. Zhang, PETSc Web page, 2009. <http://www.mcs.anl.gov/petsc>.
[60] Y. Chen, L.J. Durlofsky, M. Gerritsen, X.H. Wen, A coupled local–global upscaling approach for simulating flow in highly heterogeneous formations, Advances in Water Resources 26 (2003) 1041–1060.
[61] N. Zabaras, D. Samanta, A stabilized volume-averaging finite element method for flow in porous media and binary alloy solidification processes, Advances in Water Resources 60 (2004) 1103–1138.
[62] M.A. Christie, M. Blunt, Tenth SPE comparative solution project: a comparison of upscaling techniques, SPE Reservoir Evaluation and Engineering 4 (2001) 308–317.
[63] X. Ma, N. Zabaras, Kernel principal component analysis for stochastic input mode generation, Journal of Computational Physics, under review.